2021

Large-Scale Replication of Anisotropic Nanostructures For Development of Anti-Reflective Surface on Glass

Amritha Narayanan
amritha1311@gmail.com

ABSTRACT

LARGE-SCALE REPLICATION OF ANISOTROPIC NANOSTRUCTURES FOR DEVELOPMENT OF ANTI-REFLECTIVE SURFACE ON GLASS

Amritha Narayanan, M. S.
Department of Electrical Engineering
Northern Illinois University, 2021
Venumadhav Korampally, Director

Improvement in the anti-reflection coating (ARC) technology is considered as one of the most important advances made in modern lens design for microscopes, cameras, and other optical devices. In the semiconductor industry, integrated circuit (IC) chip manufacturers face increasing challenges posed by reflections from the underlying substrate during photolithography, a process used for the fabrication of ICs. Without the introduction of ARC materials, the nanoscale circuitry that drives today's modern electronic devices would not be possible. Despite its technological significance, real materialistic solutions with low refractive index (less than 1.3) are limited. Anti-reflection (AR) coatings today are most often based on single or multilayer interference structures with alternating high and low refractive structures. An alternate to this would be a graded refractive index surface, which can be observed in nature on the corneal surfaces of a moth eye and night-active butterflies. This research focuses on biomimicking these anisotropic pillar-like nanostructures, similar to the ones seen in a moth eye. Furthermore, conventional fabrication technologies suffer from being time consuming, expensive, and restricted to small areas. A major challenge remains in fabricating these arrays on large-area substrates using a simple and scalable technique. This work proposes a novel method of an easy roll-to-roll technique of using molded masks with ink to stamp the structures on large-area substrate like glass in the nanoscale. It exploits

the usage of a solution-processed nanotransfer printing technique for rapid and high-throughput fabrication of heat-stable and mechanically robust nanostructures.

NORTHERN ILLINOIS UNIVERSITY

DEKALB, ILLINOIS

MAY 2021

LARGE-SCALE REPLICATION OF ANISOTROPIC NANOSTRUCTURES FOR DEVELOPMENT OF ANTI-REFLECTIVE SURFACE ON GLASS

BY

AMRITHA NARAYANAN

A THESIS SUBMITTED TO THE GRADUATE SCHOOL

IN PARTIAL FULFILLMENT OF THE REQUIREMENTS

FOR THE DEGREE

MASTER OF SCIENCE

DEPARTMENT OF ELECTRICAL ENGINEERING

Thesis Director:

Dr. Venumadhav Korampally

ACKNOWLEDGEMENTS

Foremost, I would like to express my sincere thanks to my advisor, Dr. Venumadhav Korampally, for his thorough guidance and support of my master's study and research. I owe him a great debt of gratitude for introducing me to the latest trends in the world of micro- and nanotechnology. His constant guidance has helped me in all times of research and writing of this thesis. I would also like to sincerely thank my thesis committee members, Dr. Mohammad Moghimi and Dr. Donald Zinger, from the Department of Electrical Engineering, NIU, for their valuable suggestions and feedback during the course of this work.

I would like to acknowledge the Department of Electrical Engineering, NIU, that provided the necessary facility, specifically the Microelectronic Research and Development Laboratory (MRDL) where most of my research work was carried out. I would like to specifically appreciate my research colleague, Giridhar Sankabathula, who had initially trained and set me up in the Clean room, and Steven Binderup for his extensive assistance in training and handling the equipment at the MRDL.

Last but not the least, I would like to thank my family: my parents, Mr. Sankara Narayanan and Mrs. Usha Narayanan, for providing me with all the strength to come to the United states to pursue my education. My acknowledgments would be incomplete without thanking my dear friend and colleague, Sneha Ramesh, for always believing in me and supporting me whenever and wherever required.

DEDICATION

To my loving parents and my baby nephew, Atharv

TABLE OF CONTENTS

Page

Chapter Page

LIST OF FIGURES

Page

Page

Page

Page

Page

LIST OF TABLES

Page

1. INTRODUCTION

Improvement in the anti-reflection coating (ARC) technology is considered as one of the most important advances made in modern lens design for microscopes, cameras, and many other optical devices. In fact, without the introduction of ARC materials, the nanoscale circuitry that drives today's modern electronic devices would not have been possible. Today, anti-reflective coatings (ARCs) have extended conventional lithography processes far beyond their original limitations that has enabled the production of smaller and smaller integrated circuits (ICs). Without ARC, the devices we use for communication and entertainment could not be as small, fast, and powerful as they are today. To understand how ARC enables this trend, we need a basic understanding of the process used to make the Integrated circuits that power today's devices.

Individual device components such as memory chips and CPUs are known as integrated circuits or ICs. They are manufactured in layers on a silicon wafer and each layer of the microscopic circuitry is created using a complex process called photolithography. Photolithography involves several basic steps. At first, a photosensitive material called photoresist is spin-coated onto the surface of a silicon wafer. It is then exposed to an ultraviolet (UV) light source that shines through a mask that has a pattern of openings that allow the light to pass through to the photoresist-coated silicon wafer. The photoresist is chemically changed wherever it is exposed to light so that areas of the patterned photoresist can be removed according to a desired circuit pattern. Now, during the exposure step of the lithography process, any light that passes through the photoresist can be reflected by the underlying layers. In earlier generations of the

lithography process, the patterns formed were much larger, so reflections from the underlying layers were not problematic. In today's advanced processes where feature sizes are measured in nanometers, these same types of reflections would ruin the patterns in the photoresist. In some cases, the reflected light from the exposure bounces up and disrupts the incoming light, causing an interference pattern known as a standing wave. As its name implies, a standing wave will create an undesirable wavy profile along the walls of the exposed photoresist. Reflections become even more problematic when patterns must be created on top of the existing structures. These various peaks and troughs can reflect the light at different angles, resulting in a phenomenon known as reflective notching. This is when anti-reflective surfaces play a major role in mitigating such problems.

There has been extensive research still working on finding a solution in being able to produce a good anti-reflective surface. There is even more important interest in being able to fabricate it with a very low refractive index and being able to replicate it over larger areas, along with the simple steps required in fabricating the same. The next section gives a general idea of how this report is sectioned into different chapters and an overview of each of those chapters in how this research work has been able to bring about this idea to work.

1.1 Thesis Overview

The purpose of this research work is to study and investigate the methodology for production of anti-reflective nanostructures on a substrate like glass with a low and/or a graded refractive index for a broadband of wavelengths of light based on biomimicking moth-eye corneal surfaces. These nanostructures are made on conventional and inexpensive silicon substrates using

simple self-assembling techniques and nanofabrication procedures, which have been exploited extensively for the purpose of this work. This thesis is divided into seven chapters.

The first chapter introduces the research topic by explaining the importance of anti-reflective surfaces, along with the trend of the fabrication methodologies from the past to present with collaborative literature work presented in Chapter 2. It also provides the governing theoretical background and equations for achieving the desired end goal of this research.

Chapter 3 starts with the detailed explanation of each of the fabrication modules, starting from discussing about the nanosphere lithography technique utilized for the self-assembling technique of getting ordered monolayers for the point of creating an oxide mask layer for desired patterns while etching.

Chapter 4 enumerates the kinds of etching processes, with the main focus being towards reactive ion etching in aiding with the fabrication procedure for acquiring the desired nanostructure pattern. It includes with all the results obtained throughout the course of this research work. In Chapter 5 we propose a novel method for assisting with large-scale replication of the results obtained in the previous chapter, using inexpensive and an easy roll-to-roll technique. Its emphasis is on the process recipes and the factors that affect the replication process.

Chapter 6 has all the required proof-of-concept simulations done with the help of a finite-difference time-domain (FDTD) solver in Ansys Lumerical Inc. software for better studies and analytics. Chapter 7 concludes with the summary of the findings presented with this thesis along with future work that could be done as part of an extension to this research.

1.2 Literature Review:

There have been exceptional improvements in the field of optics for anti-reflection owing to its importance in many key applications. Initially, the idea of achieving anti-reflection was quite incidentally construed by Lord Rayleigh in the 19th century when he observed that the tarnishing on glass increased its transmittance instead of reducing it. This led to the strategy of achieving anti-reflectivity by gradually increasing the refractive index [1]. However, the introduction to ARC was produced back in 1817 by Franhofer when he noticed reflections reduced as a result of etching a surface in an atmosphere of sulfur and nitric acid vapors. A few years later, the phenomenon of ARC was described as the destructive interference between the light reflected from a surface of a substrate and the light reflected from a thin film that is coated on that substrate [1]. This means that the relative phase shift between the beam reflected at the upper and the lower boundaries of a thin film is 180̊, which cancels out both the beams before they exit the surface.

The application of thin-film coatings for the purpose of anti-reflection is also very well-known. The reflected light at the interface of two optical media with different refractive indexes is known to reduce with the addition of a thin-film optical coating at the interface, having a refractive index between that of the two optical media [1]. Yoldas [2] prepared a porous oxide layer, with a thickness of about a quarter wavelength, on glass. However, the dimension of the formed structures lies in the range from 1 to 6 um; i.e., they are approximately ten times greater than the optical wavelength and are therefore basically not suitable for the anti-reflection coating of optical lenses, mirrors etc. Producing multicoating by superimposing single coatings by McCollister et al [1] produced an anti-reflection multicoating having a gradient in the refractive index normal to the coating surface. It is also further known that having multiple layers of this anti-reflective coating

with alternate high and low refractive indexes could enhance the anti-reflective behavior even further. This can be explained by an example, where if you consider an anti-reflective coating having three layers at a glass-air interface could reduce the total intensity of 4.3% to less than 1% above the total visible spectrum [1]. Applying a coating having an optical thickness corresponding to one-fourth of the wavelength of the incident light would also reduce the reflectivity at the interface, but this would be constricted to a single wavelength of light. Furthermore, even if we did employ multiple layers of coating, actual solutions with a refractive index of less than 1.3 (for an air-glass interface) are still rare and unknown [3]. An innovation to the previously described technique utilizes the usage of nanoporous materials, where materials having porous structures of dimensions less than the wavelength of visible light is known to have an effective refractive index given by the average of the surrounding two media [1]. Hybrid configurations such as these and porous sol-gel and even optical polymer thin-film coatings with nanostructured surfaces, although enabling broadband anti-reflection properties, utilize polymer materials that suffer from strong absorbance and radiation damage when under ultraviolet (UV) light [3].

An alternate to the multilayer films can be seen in nature on the corneal surfaces of motheye and nocturnal butterfly eyes [3]. The subwavelength anti-reflective structured corneas of nocturnal moths have a graded transition of refractive index which helps in a severe reduction in the reflection of light and thereby enhancing their light sensitivity, helping them to see even in the dim starlight [4]. Surfaces tailored with these anti-reflective structures offer better advantages compared to thin dielectric films, owing to detriments in their mechanical stability, layer ablation, and tensile stress when the optical devices are used over a broad thermal range [3]. Furthermore, for avoiding scattering at the optical interface, structural dimensions have to be smaller and below

200nm of than the incident light for UV and DUV applications. Top-down technologies such as photolithography, beam lithography, nanoimprint lithography, and interference lithography are commonly used to develop these subwavelength-structured anti-reflective structures. Lohmuller et al. [3] et al discovered that metallic nanoparticles could be used as lithographic mask to etch non-straightforward structures into fused silica, resulting in quasi-hexagonal patterned, hollow, pillar-like protuberances. Raut [4] et al. were able to fabricate these structures over large areas by a distinctive approach, called sacrificial layer mediated nanoimprinting, by introducing a sacrificial layer atop a planar array of moth-eye nanostructures into microlens array, which will be explained in the coming chapters, depicted in Figure 1.1 [1].

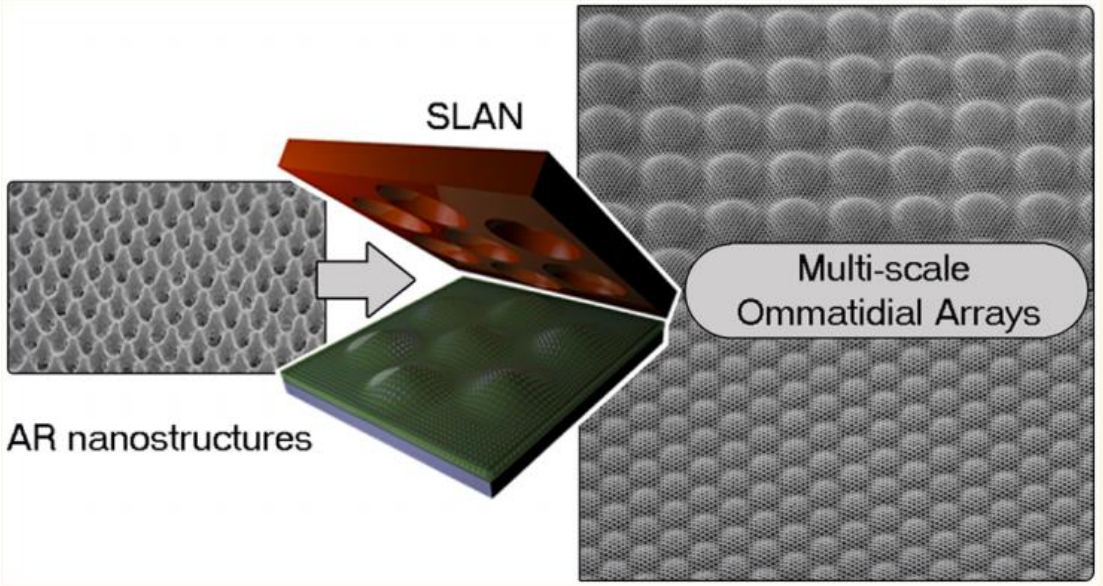

Figure 1.1 Multiscale arrays developed using sacrificial layer mediated nanoimprinting (SLAN). Source: [4].

2. FUNDAMENTALS BEHIND ANTI-REFLECTION

2.1 Optics: Reflection, Refraction, and Transmittance

By Snell's laws of reflection and refraction, the angle of incidence is equal to the law of reflection. Considering a flat surface, when a light ray strikes the surface at an angle of incidence, according to the law of reflection, the ray is going to bounce back at the same angle, the angle of reflection. The entire situation comes down to:

$$\theta_i = \theta_r$$

Now when light moves from one medium to another, a part of it gets reflected, some gets absorbed, and the rest gets transmitted. And that is where we get the color of objects and what colors they actually have. Anti-reflection can be considered as a direct application of the interference of light. In typical imaging systems, anti-reflection is used to improve efficiency since less light would be lost due to reflection. In complex systems, like telescopes and microscopes, the reduction in reflection substantially improves the contrast of the image by elimination of stray light, more of which will be explained below. Reflection loss is a very direct loss when it comes to the production of solar cells. If the light that comes from the sun is reflected away from the cell before it even reaches it, it is lost. There is no second chance of getting back the lost light that is gone because of reflection. Therefore, it is imperative to minimize the reflection losses across a broad spectrum of wavelengths. Over the last century, many strategies and methods have been

explored to reduce reflection. Generally, the development of these anti-reflective coatings can be achieved using the two ways described in the following sections [3] [5].

2.1.1 Conventional Quarter-Wavelength ARCs

Broadly, the governing factor for developing ARC relies on the material thickness and its film thickness. The difference in refractive indexes at the material interface, say between air and a glass substrate, largely controls the optical reflection from surfaces. To optimize and maximum suppression of reflection at the interface, the refractive index of a film interposed between two materials should be the geometric mean of their refractive indexes. This is given by:

$$n = \sqrt{n_1 n_2}$$

For example, if we were to consider a photon traveling through air with refractive index of 1 and hitting a glass surface with refractive index of 1.5,the intermediate coating at the interface should have a refractive index of the geometric mean of the other two refractive indexes, resulting in approximately 1.225. Therefore, the light is being bent into the material instead of being reflected away. Subsequently, the more abrupt change in the refractive index, the higher would be the reflection. The other governing criterion is the thickness of the film should be a quarter wavelength, that is a quarter of the wavelength of the incident light at a specific location where reduced reflection is desired. This is done in order to take the advantage of destructive interference happening at the boundary; i.e., light reflected at the coating-substrate interface will be half of the wavelength out of phase from the incident light that is reflected at the coating-air interface, resulting in destructive interference and reduced reflectance [2].

The limitation to this technique is this effect is wavelength dependent. Consequently, when you look at the reflection for different wavelengths for a standard industrial application such as a solar cell, you will see that the reflections would have been reduced only for a certain wavelength. Now, if cost were not an issue, we could certainly add an additional layer at the boundary, and this would further minimize two wavelengths, and if we could have that and an infinite number of anti-reflective coatings, it would result in a broadband minimization of the reflection. But the solution and temperature requirements required for depositing these coatings on many substrate materials such as plastics make them highly incompatible [3].

Additionally, substrates that require a refractive index of 1.5 (glass) are required to have an ideal anti-reflective coating of 1.225. And materials with this low refractive index hardly exist. Magnesium fluoride with RI 1.38 is generally used as a single-layer antireflective coating, but coatings of magnesium fluoride are not appropriate for polymers because of the high tensile stress and weak mechanical properties of fluoride thin films at low polymer-processing temperatures [2].

2.1.2 Bioengineered Moth Eye ARCs

The perfect example for ARCs can be found around us in nature. For many years, eyes have been of ineluctable importance in many design areas. Specifically, night-vision insects like moths have pitch-black eyes that aid them in seeing in the dark and help in getting away from their predators, as seen in Fig [2.2]. They are proven to have remarkable advantages, such as greater depth of field, wide-angle view, sensitivity to motion, and negligible aberration [4]. Emulating the best strategies of nature has been a worldwide research priority of late and this has led to the evolution of a whole new branch of science – biomimetics [5]. For instance, compound eyes of moths, when viewed at a nanoscale, have a curvilinear design of hexagonally packed microlenses,

called ommatidia, which focus the incident light to the internal photoreceptors. And each ommatidium is further textured into patterns of hexagonally packed, subwavelength anti-reflective nanostructures that produce a gradual transition of the refractive index at the interface of two media [4]. In other words, the refractive index is non-uniform. This non-uniformity arises because the refractive index is higher at the axis of the core (the center) and continuously reduces as you radially move away from the axis. Therefore, instead of going the abrupt way, we head in a gradual way in the perspective of a photon in light. And this must be in the order of the wavelength of light and that means in nanoscale. That is why nanostructures can suppress reflection or a broadband of wavelengths and not just one. In fact, this represents the use of replacing the infinite layers of infinitely thin ARCs, as discussed in the Chapter 1.

The experimental reflection measurement is complemented using a theoretical calculation using a rigorous coupled wave analysis (RCWA) model [5]. In this mode, a coordinate system is set up with *z*-axis perpendicular to the nipple structures of the moth eyes so that the array troughs are at z=0 and the nipple peaks at $z=h$. The nipple arrays are then divided laterally into N= 100 horizontal layers each having thickness of the *z*-coordinate z^* and radius r^* of each layer as given below:

$$Thickness = \ h \ / \ N$$

$$Radius, r^* = r\sqrt{1 - (z^* \ / \ h)} \ \text{, where } 0 \leq z^* \leq h$$

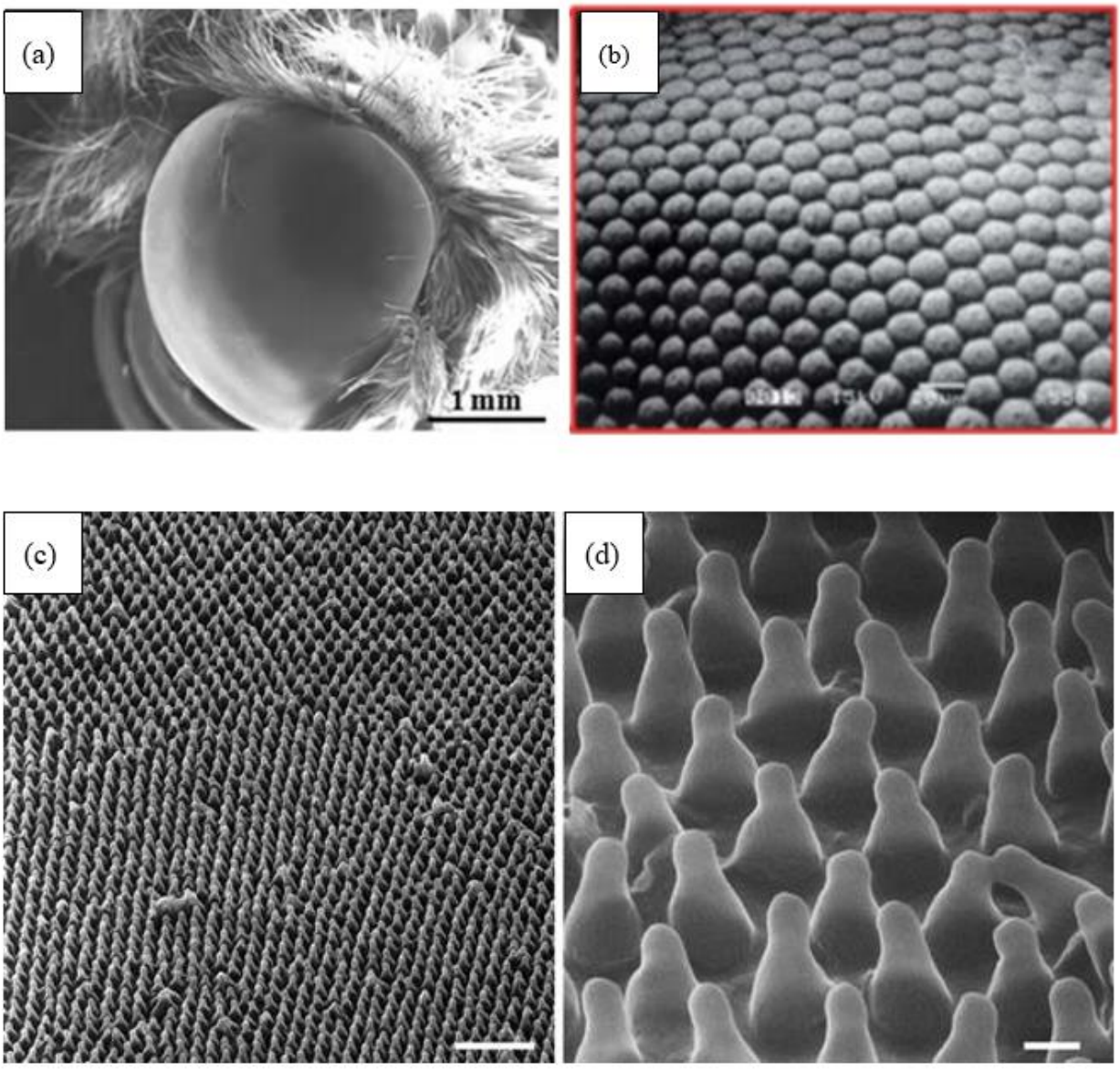

Figure 2.1 SEM-magnified image of a moth eye drilled down from mm range (a) to um range (d) showing hexagonal array of nanostructures.

The nipple lattice is assumed to be hexagonal and the distance between the centers of the neighboring troughs would be given as $\sqrt{2D}$, where *D* is the diameter of the templating spheres. Therefore, the horizontal layer at level *z** contains a fraction *f(z*)* of silicon with complex refractive index $N_{Si} = n + ik$ (*n* and *k* are optical constants obtained from literature) and a fraction *1− f(z*)* of air with refractive index $n_{air} = 1$. The hexagonal structure of the nipple arrays leads to the formula:

$$f(z^*) = \left[\pi(r^*)^2/\sqrt{3D^2}\right]$$

Based on the effective medium theory, the effective refractive index *n(z*)* of the layer at height z* could be approximated by:

$$n(z^*) = \left[f(z^*)\tilde{N}_{Si}^q + [1 - f(z^*)]n_{air}^q\right]^{1/q}, \text{ where } q = 2/3$$

We finally calculate the reflectance of the whole system by solving the Maxwell equation to express the electromagnetic (EM) field in each layer and then matching EM boundary conditions between neighboring layers for the determination of the reflectance of the system [5].

2.1.3 Reflectance Properties of Moth Eye Structures

In contrast to a moth-eye structure composed of a regular array of protruding silicon rods with finite sidewall angle, it is shown that a moth-eye structure composed of a regular array of protruding silicon rods with finite sidewall angle showed decreased reflectance and sensitivity to incident wavelength when compared to rods with perpendicular sidewalls that are completely cylindrical [6]. As the angle of incidence increases, the disparity between total reflectance of both silicon samples decreases. It can also be found out that the reflectivity at normal incidence was less than 2% for 400 to 1200nm wavelengths [6].

Figure [2.3] below from [7] displays the reflectance of a moth eye with 3300 grooves per millimetre measured at wavelengths of 647.1 and 514. 5 nm as a function of angle of incidence and polarization. These curves show that the phenomenon is surprisingly insensitive to incidence angle over a large range of angles. The discontinuities at 59. 5 ° on the 514. 5 nm curve (a) correspond to the appearance of a diffracted order and are the same as Wood's anomalies on a diffraction grating.

2.1.4 Hydrophobic Nature of Nanostructures

Along with its distinctive anti-reflection capabilities and optical performance, the nanostructures also show a distinctive anti-wettability characteristic. In other terms, they offer self-cleaning properties to enhance its practical availability. This can be proved by taking the contact angle measurements of the resulting nanostructures.

A clever analogy to this was done by Lohmuller et al. [8] to the induced super-hydrophobicity of lotus leaves that usually grow in a muddy habitat yet stays clean. It is their distinctive microscopic structure and surface chemistry that prevent the leaves from getting moistened, having water droplets formed over the surface instead of a liquid film to pick up dirt as it rolls off the leaves. And this water-repelling hydrophobic nature is solely as a result of the surface modification. This is because the water-solid contact is lowered because of the grooves between the pillars. Furthermore, the air bubbles get trapped in between these structures, forming a material-air-water interface. Thus, the wetting of these nanostructures is hindered.

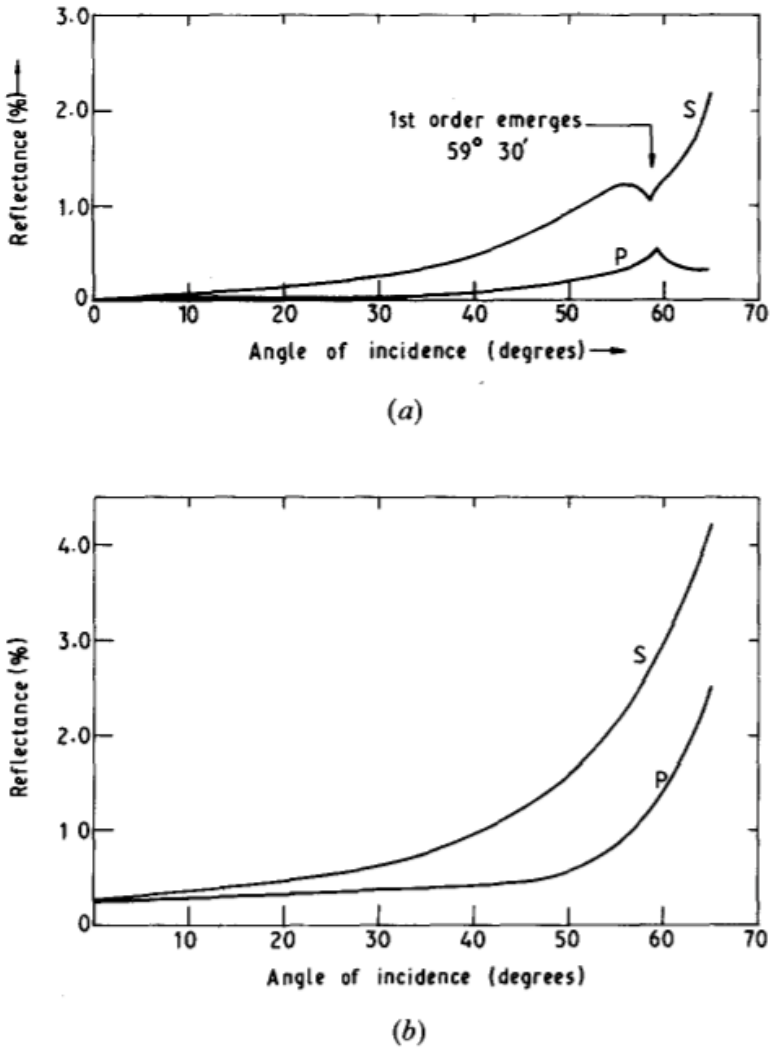

Figure 2.2 Reflection as a function of angle of incidence and polarization for 3300 groves per millimeter. Source [7].

2.2 Characterization Techniques for Anti-Reflective Surfaces

The refractive index, reflectance, and transmittance are important statistics for deducing significant conclusions about the AR structures' broadband, omnidirectional, and polarization-insensitive properties. Exsitu ellipsometers are used to analyze the optical characteristics of the films, and UV-Vis-NIR spectrophotometers are used to measure optical spectra.

Ultraviolet spectroscopy, or UV-VIS spectrophotometry, is an absorption spectroscopy or reflectance spectroscopy in the ultraviolet-visible range, which means it uses visible, near-UV, and near-IR light. White light is made up of a wide variety of radiation wavelengths in the ultraviolet (UV), visible, and infrared (IR) portions of the spectrum, despite its uniform hue. The visible range of light varies from 400nm to 800nm wavelengths.

When white light is incident on a surface, it is either mirrored or passes through a colored substance; a part of the mixed wavelengths is absorbed. The majority of the light is believed to be absorbed in complementary color to the wavelength. As a consequence, absorption at 420-430nm suggests a yellow material, which is complementary to the real absorption wavelength. A prism or diffraction grating divides a beam of light from a UV or visible light source into different wavelengths. A half-mirrored unit, called a beam splitter as seen in figure[2.3], splits the monochromatic beam into two equal-intensity beams, one of which passes along the liquid reference and the other along the sample. Some intensities are lost due to light absorption, which is determined by the detector and then compared to the reference. The system scans all component wavelengths in the visible and UV regions, ranging from 200 to 400 nm in the UV and 400 to 800 nm in the visible. If no light is absorbed by the sample at a given wavelength intensity, the sample

has the same intensity as the reference; if light is absorbed, the observed intensity along the sample is less than the reference. As a result, the absorbance can be measured using the following equation:

$$A = \log\left(\frac{intensity\ along\ reference}{intensity\ along\ sample}\right)$$

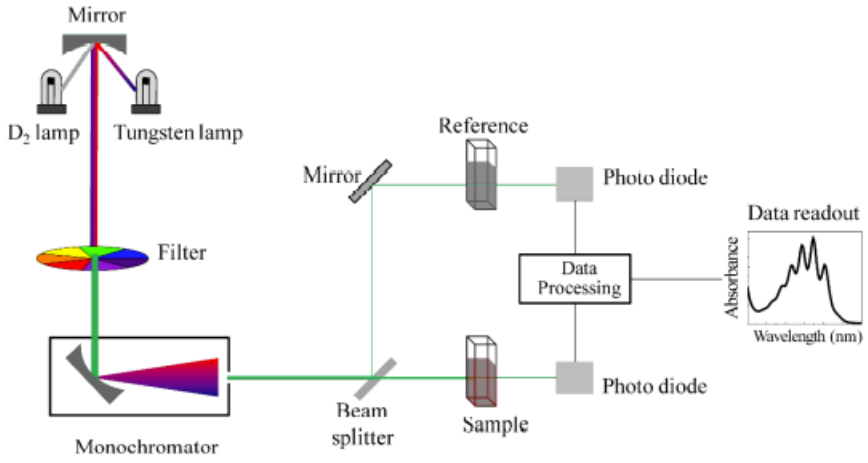

Figure 2.3 UV-VIS spectroscopy schematic diagram. Source: Wikipedia (http://www.wikipedia.org/).

The next question would be, how can we estimate the refractive index from the UV-VIS absorption spectra. Before that, we should know that refractive index is the measurement of how light propagates via a material. Keeping this in mind, we compute the percent transmittance constant (Ts) using the following equation [9]:

$$T_s = 10^{(-A)} \times 100$$

Where Ts is the percent transmittance or percent transmittance constant, and A is the absorbance calculated using the previous equation. Thus, refractive index of a sample, *n*, can be calculated as [9]:

$$n = \frac{1}{T_s} + \sqrt{\frac{1}{T_s - 1}}$$

Thus, the refractive index of the sample can be calculated using the above set of equations, which are vital for characterizing our samples for the application of anti-reflection. Although it is advantageous with rapid, straightforward data collection and accepts diverse sample types, indirect properties require advanced optical modeling.

Furthermore, there are a multitude of computational models that include refractive index computing methodologies for the various types of ARCs we have discussed thus far. For refractive index computation, these computational models rely on two of the previously mentioned landmark analytical techniques: effective medium theory and rigorous coupled wave analysis [10]. It is worth mentioning here that RCWA is more preferred as it predicts the dimensions of the crucial parameters more effectively, which eventually offers better ways of optimization and will be explained in detail in the final chapter of this work.

2.3 Goals for the Research

In our research, we would like to emulate these moth-eye-based anti-reflective nanostructures to give us a graded refractive index, that will subsequently, that which can be compatible with an overall broadband spectrum of wavelengths. Despite its technological significance, real materialistic solutions with a low refractive index (less than 1.3) are limited. An alternate to this would be the graded refractive index developed by biomimicking the moth-eye nanostructures. To fabricate them, the AR layer thickness h and the wavelength λ determine the overall reflectance.

For broadband reflection, it was earlier shown in the first chapter that $h < (\lambda/2)$ [4]. As a result, the structure's height for UV and DUV region should be at least between 100 nm and 200nm for optimal anti-reflection conditions. In moth eyes, the diameter of each of these protuberances was found to be 100 nm and are 170 nm away from one another [10]. So the height ($< \lambda/2$), inter-nipple spacing, and shape in ‘‘moth’s eye’’ structures playing a pivotal role than the width of the ‘‘moth’s eye’’ from [10].

Furthermore, conventional fabrication technologies suffer from being time consuming, expensive, and restricted to small areas. A major challenge remains in fabricating these arrays on large-area substrates using a simple and scalable technique. This work proposes a novel method of an easy roll-to-roll technique using molded masks layered with ink to stamp the structures on large-area substrate like glass in the nanoscale range. It exploits the usage of a solution-processed nanotransfer printing technique for rapid and high-throughput fabrication of heat-stable and mechanically robust nanostructures.

2.4 Fabrication Methodology

The proposed fabrication methodology in Fig. 2.4 illustrates the anti-reflective surface fabrication process. This was done exploiting a simple fabrication strategy for deposition of an oxide mask layer on top of the silicon substrate required. The aim for this step is to create a spherical array of oxide layer done through nanosphere lithography to define our èpatterns to get deep anisotropic or pillar-like protuberances completely on the surface of the substrate, thus yielding the desired moth-eye nanostructures. In obtaining these structures, we will be using reactive ion etching, which is a combination of physical and chemical etching that is done to etch the desired pattern through the silicon substrate underlying the oxide layer, again which will be

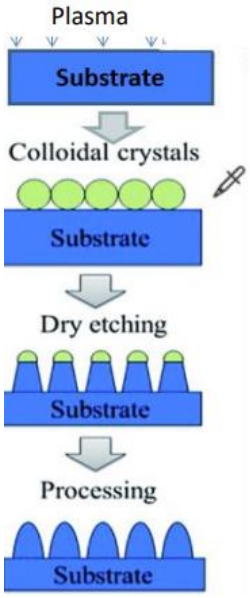

Figure 2.4 Initial fabrication schematic.

explained more in the coming chapters. After having served its purpose, we will be removing the oxide layer by use of sonication to expose the structures beneath.

Following this, we plan to achieve these results on a larger-area for real-life applications, by proposing a novel and simple roll-to-roll technique called nanotransfer lithography which will be explained in the later chapter, to aid with stamping the obtained structures onto a large area with high throughput and fidelity.

3. NANOPARTICLE MASK LAYER

Nanotechnology is being heralded as the next logical step in technological advancement, which has resulted in a significant increase in research activities relating to the growth and fundamental understanding of nanoscale processes and assembly. A lot of different techniques such as electron beam writing, mask lithography, and interference lithography techniques have been applied in realizing these anti-reflective structures [3]. The structural dimension at an optical interface must be smaller than the wavelength of the incoming light to prevent scattering from the interface ("lower wavelength limit") [3]. Very small feature sizes below 200 nm are needed for UV and DUV applications. Fabricating anti-reflecting structures with small feature sizes will require fabrication techniques that are prone to being expensive, time consuming, and circumscribed to within a small area. This chapter entails all the experimental work obtained towards getting the desired monolayered close-packed structures using oxide particles over silicon substrates using a simple self-assembling technique. For the purpose of research, we have utilized silica nanospheres of various nanometer sizes serving as an oxide layer etch mask to get the desired subwavelength nanostructures using a process that will be explained in detail in the following chapters. Along with it, this chapter also talks about another approach that uses porous based films, specifically nanoporous films (NPO) on the substrate, which have been widely used for their control over optical performance and properties.

Now coming back to obtain a large area of these closely ordered nanospheres, a self-assembly process through nanosphere lithography (NSL) techniques was utilized. NSL has piqued interest in recent years due to its compatibility with wafer-scale processes and the ability to produce a broad range of homogeneous one-, two-, or three-dimensional nanostructures [11]. We were able to optimize a simple self-assembling approach using the NSL technique, named the "vortex flow" enabled process. This technique is very much similar to the Langmuir Blodgett technique [12], although it predominantly exploits the compression of nanospheres at the air-water interface that's driven by vortex flows. This substantially eliminates the need for any sophisticated equipment or techniques.

3.1 Monolayered Self-Assembly Technique

The self-assembly deposition procedure at the interface of two different media such as air-liquid or the liquid-liquid was invented by Irving Langmuir and Katharine Blodgett [12]. This was later called the Langmuir-Blodgett technique. It is a process of preparing and transferring nanosphere monolayers from the air-liquid interface to solid substrates. The compression from floating nanospheres to closely packed monolayer is driven by a barrier called the Langmuir-Blodgett trough. With the aid of capillary and electrostatic forces, two-dimensional ordered arrays of nanospheres are trapped at the air-liquid interface. It is crucial to give the nanoparticles the required surface functionality because if they are not hydrophobic enough, they will sink into the solution's subphase, whereas too much hydrophobic trait will cause aggregation effects [13].

The nanoparticles or the nanospheres used for the experimental purposes is simply a spherical mass of silicon dioxide material that is given in monodisperse sizes usually on the scale of 200-2000nm range. They can be utilized to create well-ordered assemblies over the surface of

a substrate, typically in a hexagonally oriented crystalline pattern. These assemblies then serve the primary usage as a mask, leaving the spaces in between each particle exposed. These spheres are not actually attached to the substrate but are bound to the surface via attractive forces, further allowing us to employ dry etching techniques to etch the surface beneath before the spheres can be easily removed by sonication, leaving the processed substrate behind.

For our experiments, the self-assembling of the closely packed monolayer of silicon nanoparticles has been produced with the help of the vortex flow enabled approach recipe developed by V Korampally et al. [14]. As part of the first step in the preparation of our nanostructures, we would like to form a uniform layer of oxide on our substrate (silicon wafer). The aim of this step is to create an oxide mask on the substrate so that we can etch the silicon to get our desired nanostructures. Taking advantage of the Van der Waals forces, which is the force that arises due to the interactions between two or more permanent and/or induced dipoles, and the various interaction forces (steric and hydrophobic forces) that occur within systems of molecular/nanoscale constituents allows a uniform assembly of the silica particles onto our substrate. This ordered arrangement distributed at the air-water interface has been facilitated through the vortex flow generation within the liquid phase. This technique is illustrated below in Fig. 3.1.

3.1.1 Methodology of Self-Assembly Technique :

Initially, we choose an n-type silicon substrate which is treated with oxygen plasma to introduce hydroxyl groups upon the substrate by raising the material's surface energy. Then a thin layer of water is introduced upon the substrate that is placed in a petri-dish. A

polydimethylsiloxane (PDMS) stamp, known for its wettability modification, is stamped, and removed from the surface of the substrate to circumscribe the water within the silicon substate. Next, a solution of the silica nanospheres is prepared using the mixture of ethanol and DI water. Prior to solvent preparation, the silica nanospheres with a mean diameter of 200 to 400nm purchased from supsil, is weighed to about 30mg and transferred to a 2ml vial. These Supsil nanoparticles will be extensively used for experimental purposes.

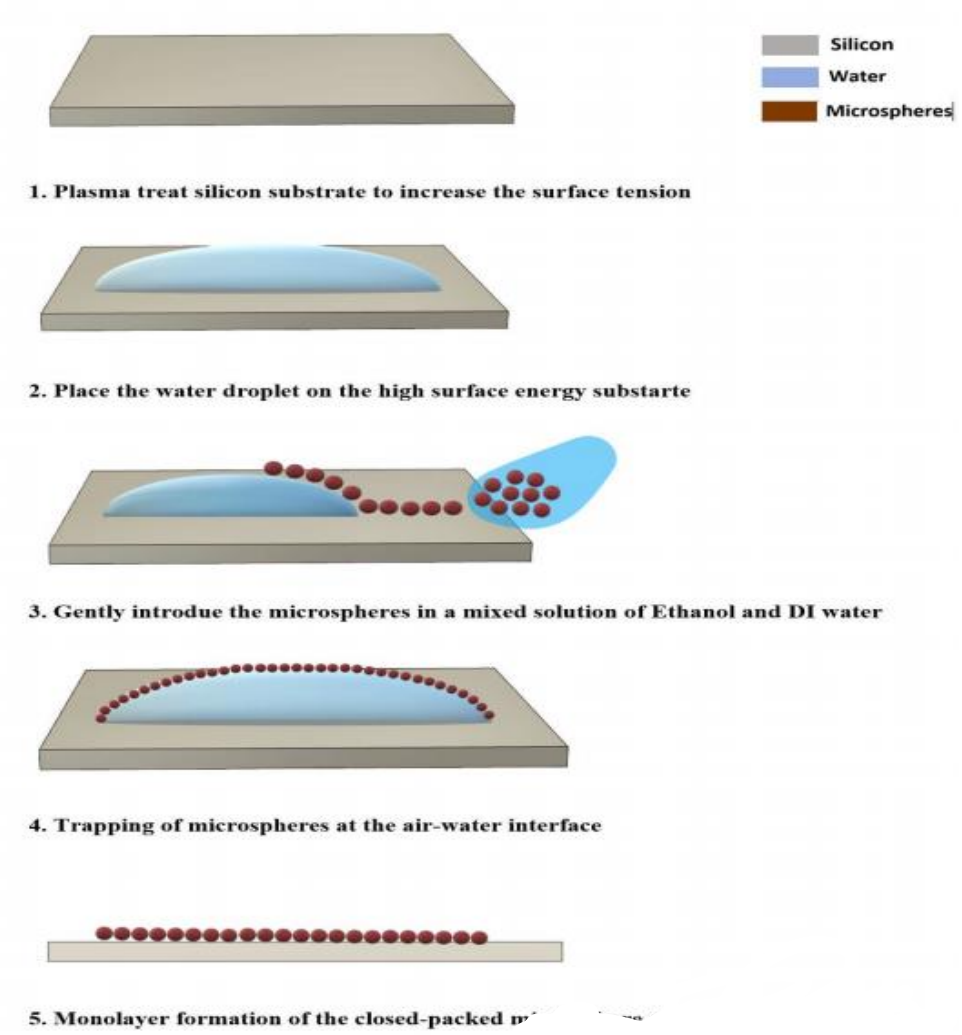

Figure3.1 Schematic of the vortex flow enable process for self-assembling of nanospheres. (1) Plasma-treated silicon substrate to increase surface tension. (2) Place water droplet on the surface. (3) Gently introduce microspheres in a mixed solution of ethanol and DI water. (4) Trapping of the beads at air-water interface, (5) monolayered self-assembly of the close-packed microspheres. Source :[15]

The particles are washed in ethanol by performing vortex mix for 2 mins followed by 15 mins of sonication for it to completely disperse into the solution. This step ensures that there are no agglomerates in the solution. The homogenous solution with nanospheres can also be filtered so that any agglomeration in the particle colloid can be reduced upon the filtration. Further, the particles are separated from the fluid through centrifugation by running at 14.5K rpm for 5 mins. Then the fluid is extracted from the vial leaving the nanoparticles that are sedimented on the ground surface. The mixture of ethanol and DI water (7:5) is added to the nanoparticle contained in a 2ml vial which is then followed by sonication to redisperse the particles into the solution, thus producing a particle colloid. This alcoholic solution incorporated with nanospheres is introduced to the water in a petri dish using a 20ul pipette to inject the nanoparticles to spread out inside the water causing the vortex flows generated by the surface tension gradients that are created across the water surface. As the vortex flows from the colloid help in transporting the nanospheres into the deposited water layer, they subsequently get trapped in the air-water interface. Upon ethanol evaporation, the transfer of monolayer arrangement of nanosphere assemblies, from the air-water interface to the wafer substrate, takes place.

3.1.2 Results and Discussion

The self-assembly deposition of nanoparticles through the vortex flow enabled process has been optimized to give a monolayered nanoparticles on a silicon substate, as seen below in Fig. 3.2 . For analysis study, magnified images of the single-array particles were taken with the help of a scanning electron microscope (SEM), a powerful tool for viewing nanoscale images with high contrast and clarity. The image in Fig. 3.3 was taken after removing the water content and curing at 100 degrees Celsius to give a monolayered assembly. The SEM image show how 400nm Supsil

particles seem to be arranged in a compact hexagonal pattern, which is ideal for a mask to etch the exposed region in between.

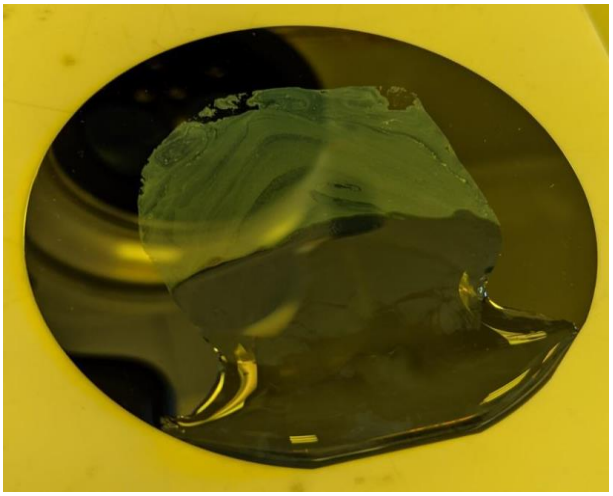

Figure 3.2. Self-assembly technique showing nanospheres evenly distributed along surface, with water collected at bottom.

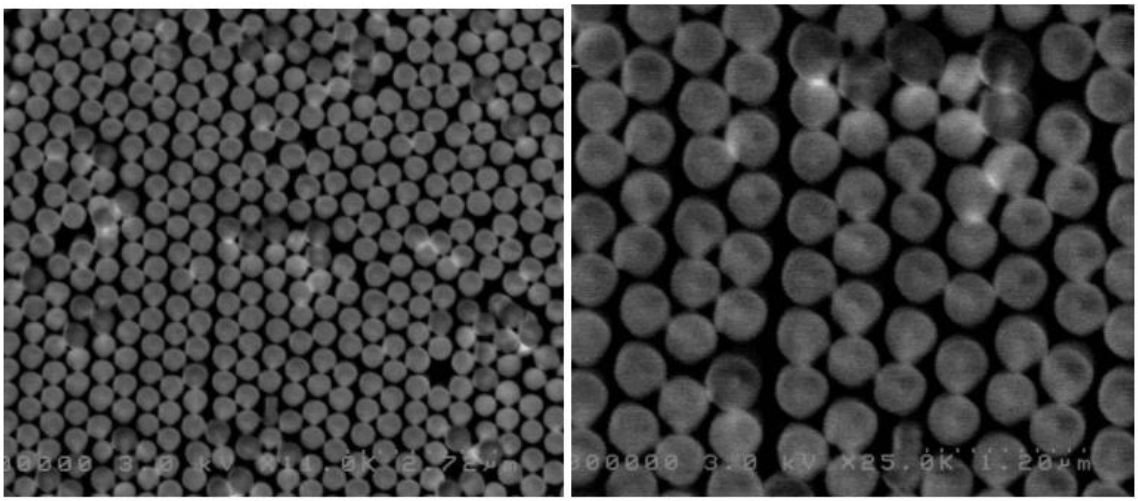

Figure 3.3 SEM image of the monolayered 400nm nanoparticle assembly at 11k and 25k magnification.

Now, as discussed earlier, although the silica particles have a densily packed structure, we will also be exploring in the coming section how the surface with nanospheres on a silicon substrate would provide a lower refractive index with the introduction of nanoporous films .

3.2 Oxide Layer on Nanoporous Organosilicate (NPO) Films

Controlling the nanostructure of materials is becoming increasingly necessary in order to produce materials with better optical, mechanical, and electrical properties [14]. The most commonly used materials for these applications are highly porous films deposited from silica-based sol–gel precursors, surfactant-templated sol–gel mesoporous films, and Organosilicate nanoporous films formed by sacrificial porogens. It is not easy to create these films with good control over their properties. The flexibility of these materials, combined with their rising demand, has necessitated the development of a new rapid, energy-efficient fabrication process. Polymer–nanoparticle composites have recently attracted a lot of attention because they provide a novel way to make multifunctional materials. The study of nanostructure self-organization through the interaction of entropic and enthalpic interactions is particularly important.

Nanoparticle–polymer composites heated above the decomposition temperature of the polymer present an intriguing, previously unexplored path, demonstrated by V Korampally et al.[14]. When the system is heated above the decomposition temperature of the polymer, the entropy of the system increases, allowing the initially confined nanoparticle to move around, as depicted in the figure [3.4] given below. The increased entropy of the nanoparticles bearing the reactive functional groups gets translated to a random movement and collisions between the nanoparticles form interparticle crosslinking and finally drive the system to a new equilibrium. This found behavior can be used to build nanoporous films with specific optical and physical

properties quickly. Over the last decade, the use of nanoporous materials in the field of photonics and sensor technologies has become prevalent. The fabrication of these films with good control over their properties is nontrivial. In more recent work done by V Korampally et al. [15] it was shown that by spatially modifying the packing density of nanoporous organ silicate (NPO) films, the refractive index of the resulting film could be modulated to have either a low (n~1.19) or high (n~1.35) refractive index. These high-quality films with pore sizes <10nm have been reported for use as anti-reflection coatings [15]. During their processing, highly regulated reaction parameters and slow healing times are required.

The recipe developed by V Korampally et al.[14] , uses Polymethylsilsesquioxane (PMSSQ) nanoparticles dispersed in polypropylene glycol (PPG) polymer. PMSSQ-based films have been chosen for their hydrophobic nature and have been a starting material for various nanoporous dielectrics, along with being inexpensive. PMSSQ is shown to have great interparticle crosslinking when dispersed in a polymer and subjected to temperatures above the decomposition temperature of the polymer (PPG), along with having low refractive index optical capabilities, which is why we have incorporated the addition of these porous films in between the substrate and the oxide layer.

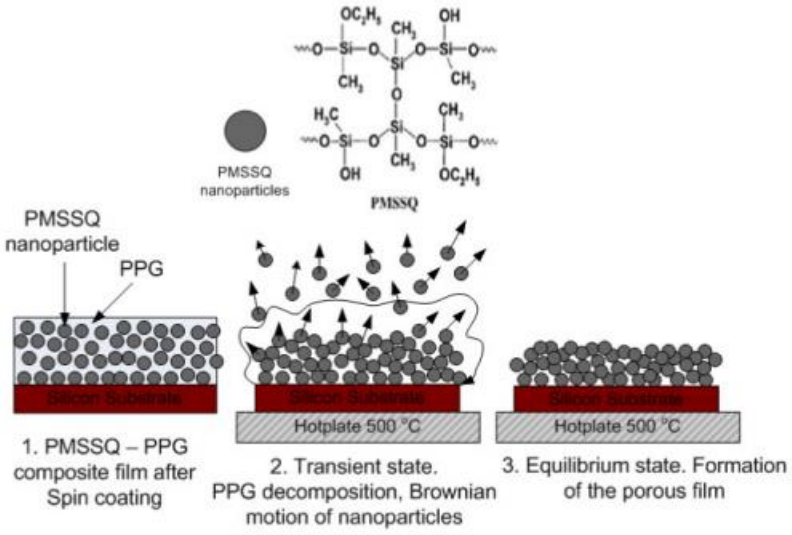

Figure 3.4 Schematic of the PMSSQ-PPG systems under high temperature curing conditions, given by [9].

3.2.1 Methodology for Fabricating NPO Films :

For the preparation of NPO films, the below recipe has been used, using a 7:3-5:5 ratio, and the films thus fabricated are called NPO7335 films in this report. A 7:3 weight ratio of PMA with PMSSQ produces a solvent; and, similarly, a 7:3 weight ratio of PMA forms nice structures dispersed with PMA to create another solvent. PPG influences PMSSQ to shape even, uniformly spaced PMSSQ nanoparticles of the same sizes distributed in PMA when both solvents are mixed together using 1:1 ratio (5:5).

After spin coating, the NPO solution applied to the silicon substrate produces a PMSSQ-PPG composite film. By exposing the film to high temperatures (400 – 500° C), the PMA solvent, which is a residue in the process, will evaporate, resulting in a transient state of Brownian motion of nanoparticles that eventually reaches equilibrium, resulting in the formation of nanoporous

films. Therefore, we can see an instant puff of PMA solvent evaporation followed by PPG polymer phase at a slower rate, leaving behind solid PMSSQ nanoparticle films. In Fig. 3.5 shows the water contact angle measured on the NPO film coated on the substrate. Here, we can see that the surface has changed from being hydrophilic to a well-hydrophic surface with less contact angle between the water and the surface as it's spread evenly on the surface.

Another approach commonly used in this thesis is the deposition of polystyrene nanospheres, a commonly available material. Although it should be noted that Sio2 (glass) nanoparticles can be subjected to high temperatures, polystyrene (plastic) nanosphere assemblies can be heated below 100 C, as there is a risk of the assemblies getting melted. For deposition of polystyrene nanospheres, we will be utilizing the same self-assembly enabled vortex flow method. However, the measurement was done by mixing 250ul of the polystyrene solution and 250uL of ethanol, making a 1:1 aqueous solution. This solution is then dispersed carefully on a plasma-treated substrate in yielding monolayered closely packed assemblies.

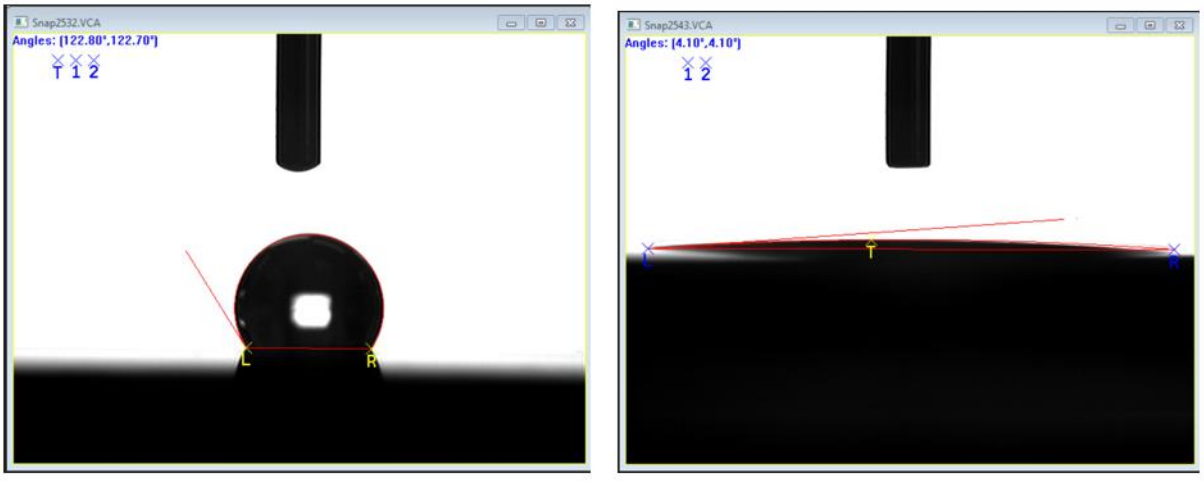

Figure 3.5 Contact angle measurement (a)before and (b) after coating with NPO film.

We will be using polystyrene assemblies while experimenting with the NPO films and as an oxide layer itself, explained in the coming chapters. After looking into the lithography techniques done in obtaining the oxide layer, we will be heading down to the next step for patterning the desired structures by a process called etching.

4. REACTIVE ION ETCHING

Etching, in simple layman's terms, would be the removal of unwanted materials from a surface to get a desired pattern. The main parameter or controls to investigate while etching would be the etch rate, which gives the rate of change in thickness of the substrate that is getting etched. The second parameter is the selectivity of the reactant that is used to etch, and the third parameter is the etch profile that it yields. There can be two etch profiles that can occur, one being isotropic, where the substrate gets etched at the same rate in all directions. And the other being anisotropic etch profile, which has a directional or a vertical etch. This is illustrated as given below in Figure 4.1.

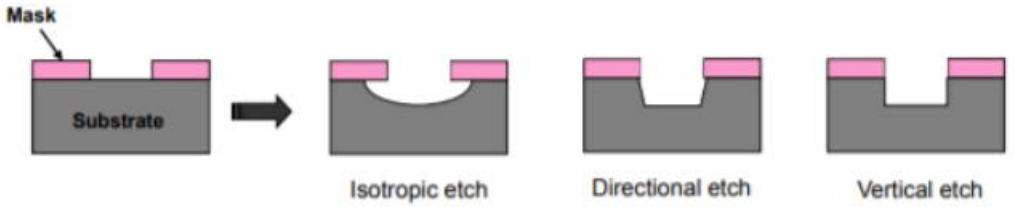

Figure 4.1 Kinds of etch profiles [16].

Etching can be achieved in one of two ways, wet and dry etching.

4.1 Wet Etching

In this type of etching, the etchant that is used to etch the substrate is a liquid chemical, thus the name wet etching. This usually has three major process stages involved, the first being diffusion of the reacting ions from etchant solution towards the exposed film on the wafer through the surface boundary layer. This is illustrated by the below diagram in Fig. 4.2.

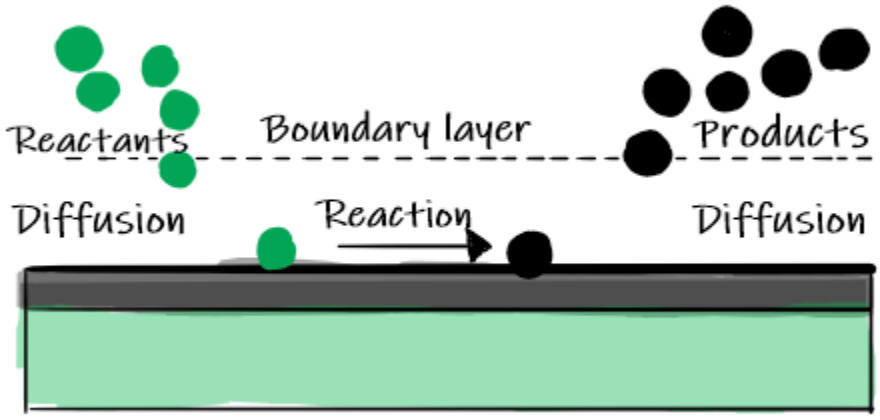

Figure 4.2 Wet etching process.

The second stage is the formation of soluble or/and gaseous by-products through the chemical reaction between etchant and the exposed film. The final stage is diffusion of reaction by-product from the surface of the wafer through the boundary layer into the bulk of the etchant solution [17]. The advantage of wet etching is that it is the simplest and the most economical technique. but it is highly selective and difficult to control. This kind of etching yields an isotropic etch profile, as explained earlier.

A process was developed by Buchine et al. [18] for the application of fabricating nanowire arrays, where they deposit nanoparticles of silicon dioxide (SiO_2) and pattern a metal film of silver (Ag) of 40nm by sputter deposition onto the substate such that the metal is present and touches silicon where etching is desired and is blocked from silicon elsewhere. For the etching process, they submerge the metallized substate into an etchant aqueous solution comprising a 4 by 49 % volume of hydrofluoric acid (HF) and an oxidizing agent such as hydrogen peroxide (H_2O_2). The etching process was initiated at the Ag/Si interface. They were able to produce nanowires with controlled diameter and length. The purpose of using nanoparticles is to block the silver from

touching the silicon, where etching is not desired, and thus getting well-defined nanowires. The dimensions of the nanoparticles or the oxide mask layer play a crucial part in influencing the dimensions and the shape of the resulting one-dimensional nanowires. However, agglomeration of the SiO_2 particles resulted in nanowire dimensions on the order of a single agglomerate.

4.2 Dry Etching

In dry etching, plasmas or etchant gases remove the substrate material. The reaction that takes place can be done utilizing high kinetic energy of particle beams, chemical reaction, or a combination of both.

4.3.1 Chemical/Reactive Dry Etching

Chemical dry etching (also called vapor phase etching) does not use liquid chemicals or etchants and this process involves a chemical reaction between etchant gases to attack the silicon surface. The chemical dry etching process is usually isotropic and exhibits high selectively.

4.3.2 Physical/ Ionic Dry Etching

Physical dry etching requires high-energy kinetic energy (ion, electron, or photon) beams to etch off the substrate atoms. When the high-energy particles knock out the atoms from the substrate surface, the material evaporates after leaving the substrate. There is no chemical reaction taking place and therefore only the material that is unmasked will be removed. The physical reaction taking place is illustrated in Fig. 4.3b. Anisotropic dry etching can etch with finer resolution and higher aspect ratio than isotropic etching. Due to the directional nature of dry etching, undercutting can be avoided. Fig 4.3a shows a rendition of the reaction that takes place in chemical dry etching. Some of the ions that are used in chemical dry etching is tetrafluoromethane (CF4), sulfur hexafluoride (SF6), nitrogen trifluoride (NF3), chlorine gas (Cl2), or fluorine (F2).

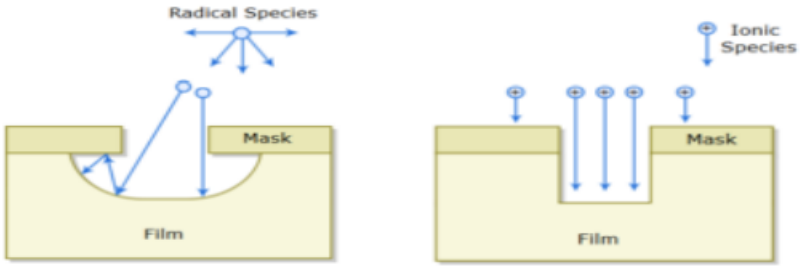

Figure 4.3(a) Reactive vs (b) ion etching. Source: [11].

4.3 Reactive Ion Etching (RIE)

This uses both physical and chemical mechanisms to achieve high levels of resolution. The process is one of the most diverse and most widely used processes in industry and research. Since the process combines both physical and chemical interactions, the process is much faster. The high-energy collision from the ionization helps to dissociate the etchant molecules into more reactive species. In the RIE process, cations are produced from reactive gases that are accelerated with high energy to the substrate and chemically react with the silicon. The typical RIE gases for Si substrate are CF4, SF6 and Cl2. As seen in Fig 4.4, both physical and chemical reactions are taking place.

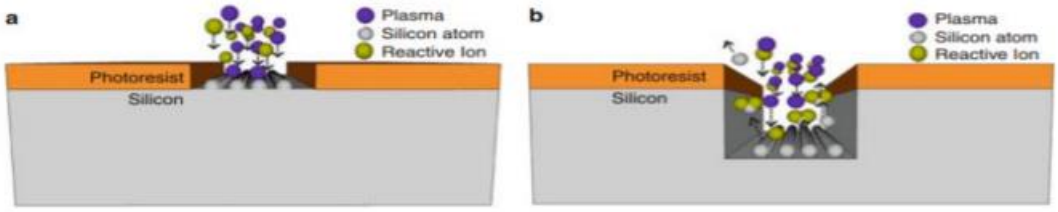

Figure 4.4 RIE (a) before and (b) after the etching process.

Because of their high etch rates, normally hydrogen- and halogen-based (i.e., F, Cl and Br) plasmas are used for the RIE of Si, as the etch products are volatile (e.g., SiH4, SiF4, SiCl4, and SiBr4 respectively). F-based plasmas are generally used for isotropic etching; Cl- and Br-based plasmas such as Cl2 are primarily used to achieve anisotropic etch profiles. Therefore, mixed molecules (e.g., CCl2F2) and gases (e.g., SF6/Cl2, CF4) containing halogens are often used for anisotropic etching. By changing the relative atom density, e.g., the F/Cl ratio in the feed gas, it is possible to vary the trench profile.

Having RIE in our experiments would help us in obtaining the desired conical nanostructures that we were trying to emulate. The plasmas used to strike for the reactive ion etching can be generated generally with two techniques, such as inductively coupled plasma (ICP) and capacitively coupled plasma (CCP). Before going into detail, the term “plasma” must be explored first. Plasma is like the fourth state of matter, following solid, liquid, and gas. It is an ionized gas, a gas into which sufficient energy is provided to free electronics from the atoms or molecules. This allows both ion and electron species to coexist. Indeed, the process for the former technique (ICP) required equipment not set in the MRDL, so we would resorted to the latter technique (CCP) for the rest of our experiments.

4.4.1 Inductively Coupled Plasma (ICP) – RIE

In inductively coupled plasma-RIE process, an RF (radio frequency) power source is used to apply energy inductively in a time-varying manner, resulting in a shift in magnetic field. A very high density of plasma can be generated by inductively coupling the RF antenna and plasma. The RF antenna generates an alternating magnetic field and causes an electric field that contributes to electron excitation. The ionization of gas molecules and atoms is caused by collisions between electrons and slow-moving ions. As a consequence, the guided ions etch away the target material by reacting chemically with the substrate. The difference between both these processes is that the electron density for ICP is higher and would give faster etch results.

4.4.2 Capacitively Coupled Plasma (CCP)- RIE

At MRDL, we have the CCP-RIE system. Capacitive coupled plasmas are where the plasma is sitting between the electrodes with a sheath on both sides, so the plasma is driven by radio frequency (RF) currents going through the electrodes. We have the RF supply; here these are RF current going through the top electrode it goes through the sheath region, through the plasma, and then out on the other side. The RF current will be keeping the plasma running. It should be noted that we never use DC supply for etching because of damage issues to the system itself. For RF, 13.56 megahertz is the industrial plasma frequency set by the Federal Communication Commission (FCC).

RF current flow determines the sheath voltage. That is, the electrons carry the RF current in the plasma region, where the electrons are mobile and carry the current. But at the two sheath regions, there are not enough electrons to carry the RF current. Therefore, the RF current gets across this region by displacement current to get across the capacitor, to build up charge on one side of the capacitor, and then on the two plates of the capacitor. The charge on one side induces

charge on the other side, thereby creating an oscillating charge across the capacitor. Thus, the desired highly anisotropic nanostructures can be obtained using this directional bombardment of plasma.

4.4 Investigation on Developing Anisotropic Etched Profiles

Plasma etching is extremely sensitive to many variables, making etch results inconsistent and irreproducible. Therefore, important plasma parameters and their influences on mask materials will be treated. The result of an RIE process depends in a non-linear way on a great number of parameters. Therefore, a careful data acquisition is necessary. This part entails a report of such findings and data.

The study has focused on the influence of different gases introduced into the etching process of silicon. The etch anisotropy attained using atomic chlorine has been a well-known etchant process. Although, this would have made it easier and faster in obtaining the black anti-reflective silicon nanostructures, we were in short supply of Cl2 gas and had to reach out for other alternate solutions for the same.

The available gases studied are CF4, SF6 and O2. It is demonstrated that with fixed RF power and chamber pressure, addition of these gases can change the profile of the etched silicon tips from being very sharp to being very blunt. The tip height and radius can be fine-tuned.

Let us look closely at how the free radicals that formed in the CF4 plasma reacts with silicon film. Electrons react with CF4 to produce fluorine and CF4 radicals. If you have a silicon substrate, fluorine can react via this reaction:

$$e^- + CF_4 \rightarrow CF_3 \cdot + F + e$$

$$Si + 4F \rightarrow SiF_4$$

The by-product of the reaction is the gas silicon tetrafluoride (*SiF4)*. This species easily evaporates into the gas phase and leaves the surface exposed for more silicon to be etched. It is important in the etch process that by-products of etch as well as any unreacted etchants be removed from the surface for the etching to continue. In some etch processes, reaction products can be used to passivate surfaces that you do want to etch. Passivation shields surfaces from chemical attack. This process enables very highly selective and anisotropic processing.

Other observations that can be noted are that the sidewall verticality could be well controlled by the flow rate of added O2 gas. Oxygen flow plays a crucial role in isotropic etching of silicon. In addition, the height of silicon tips as well as the sharpness of the tips are found to be controlled by adding Ar gas into the plasma [17]. Now, in the coming sections we show our experimental plans followed by the results achieved when applying CCP-Reactive ion etching with various etch recipes for getting our desired patterns.

4.5.1 Study of Etching with Sio2 Particles

Initially, the study was done with 8sccm mass flow rate of CF4 on 1000nm Supsil particles, deposited as mentioned in the earlier section, at 300W RF power and setting 350mTorr of internal pressure used to spark the plasma. The first image shown in Figure 4.5 shows the top-view SEM image of 1000nm Sio2 particles. It can be observed that the particles have not formed well-ordered assemblies, which could be due to the possibility of having hydrophobic terminated or the methyl-acrylate-treated batch of particles that were ordered through Supsil. The second image shows the side-view profile after 5 mins of etching, where it can be seen that the surface below the particles have started to etch, giving it a bud-like projection in Figure 4.6. The particle size has been reduced

and also an average of 350nm deep nanostructures can be observed. This was an initial experiment for getting to understand more about the RIE system operation, and how the anisotropy profile would look. For the rest of our experiments, we used 200-500nm nanoparticle structures, and studied their etch profiles, and developed etch recipes.

Next, the trial with 400nm SiO2 Supsil nanoparticles was carefully carried out, which were deposited on the silicon substrate. For developing anisotropic nanostructures, 22sccm of CF4 with 300W RF power supply and internal pressure set to 350mTorr was used. Here we have left out oxygen to study the etch profile without oxygen plasma, thereby helping to slow particle shrinkage.

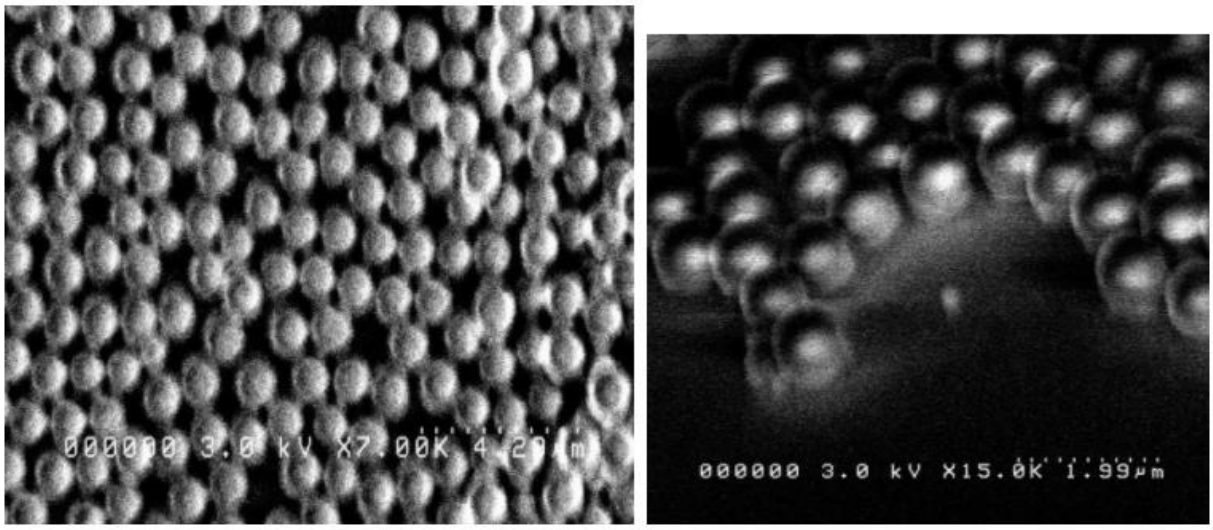

Figure 4.5 Top image showing top view of 1um Supsil assemblies, top right image showing side view of 5 mins etched sample of CF4 1um assemblies.

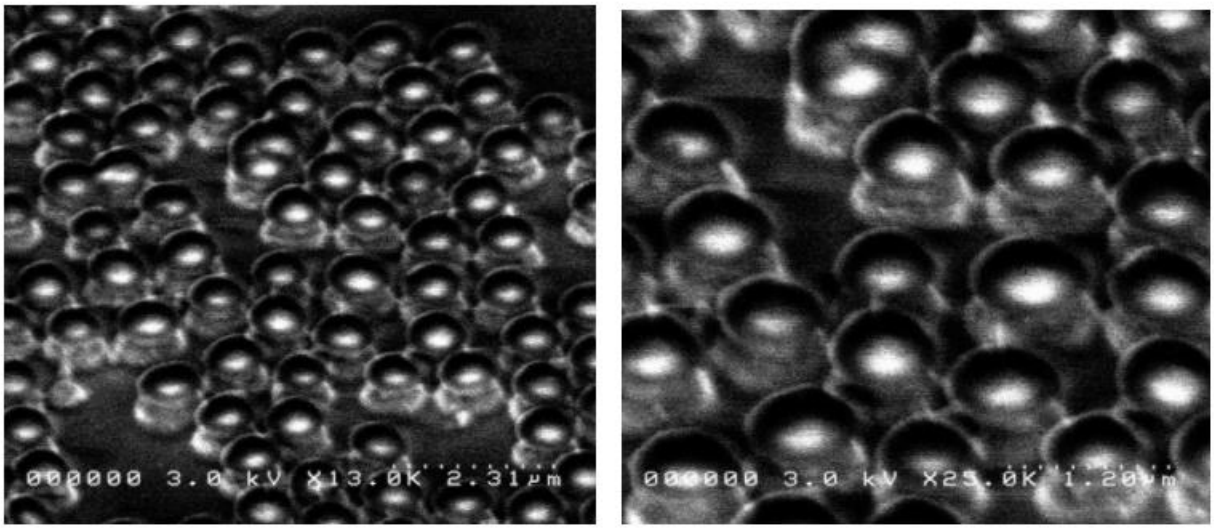

Figure 4.6 Side angle view after 15 mins of CF4 etch at 6k, 13k and 25k magnification.

The resulting structures were imaged using the scanning electron microscope (SEM) for high-quality nanoscale imaging. In Figure 4.7a we can see the well-ordered hexagonally arranged monolayered assemblies of the 400nm Sio2 particles dispersed on silicon substrate, followed by 10 mins of etching recipe, defined previously, for a duration of 10 mins in Figure 4.7b. The spheres look like they have etched, as one can observe the spaces between the spheres have increased, resulting in an etch rate of 30nm/min. The third image in Figure 4.7c is the result of etching at 10+30 mins with the same recipe, where the surface is completed overetched, and the spheres have been etched away completely, along with the silicon area underneath it. Here, we can understand what etching for a long time with CF4 etchant gas, although with less mass flow, would result in.

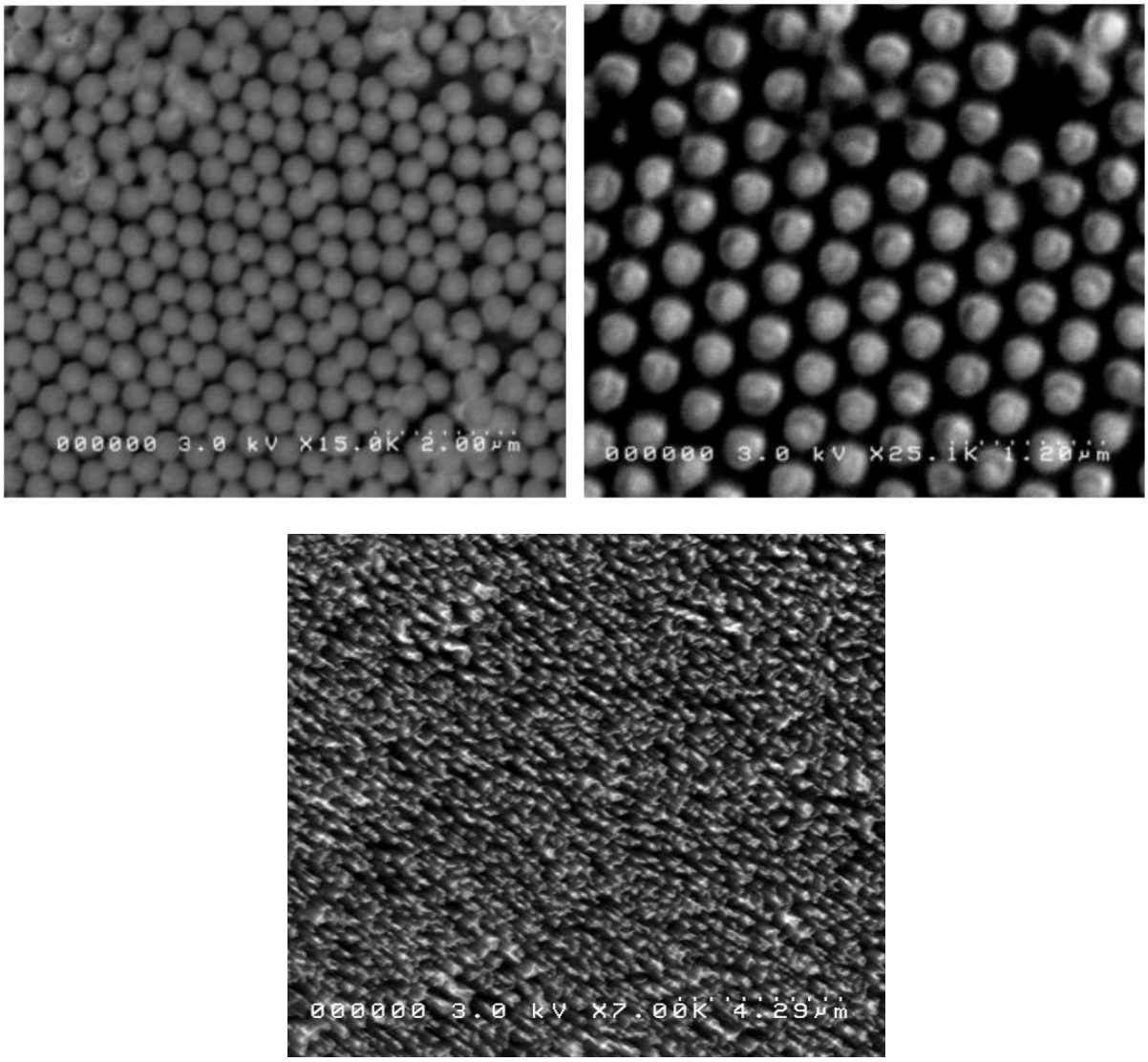

Figure 4.7 From top left image showing hexagonal ordered arrangement of 400nm SiO2 particle at 0 mins ; Top right image showing the top view after 10 mins etch and (c) bottom image showing top view at 40 mins etch using CF4.

In Figure 4.8, we can see the side profile at approximately 45 degrees of side tilt of the same samples as above, giving us non-straightforward etch profile at 10 mins of etch, with a reduction of the particle diameter to around 334nm. The processed silicon substrate surface of the side view after the etching process was somewhat rough visually. The image in Figure 4.9 shows

the actual image that was taken using a phone's flashlight. This indicates that light that is incident (from the flashlight) was getting reflected back into our eyes, showing maximum reflection.

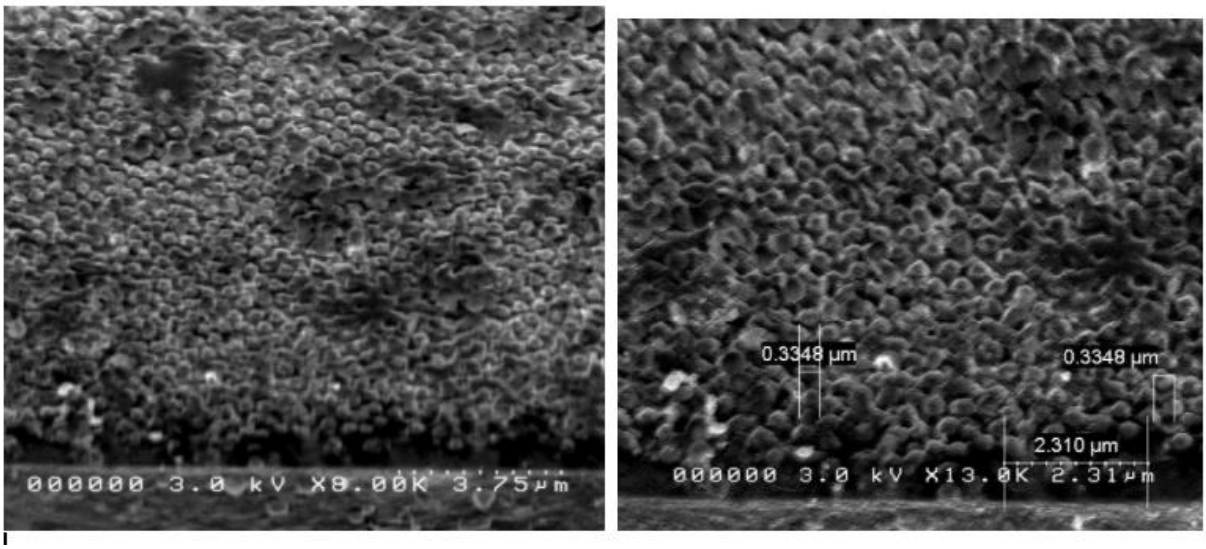

Figure 4.8 Both the images show the side view image of 400nm, CF4 etched for 10 mins at 8kx and 13kx magnification with scaling.

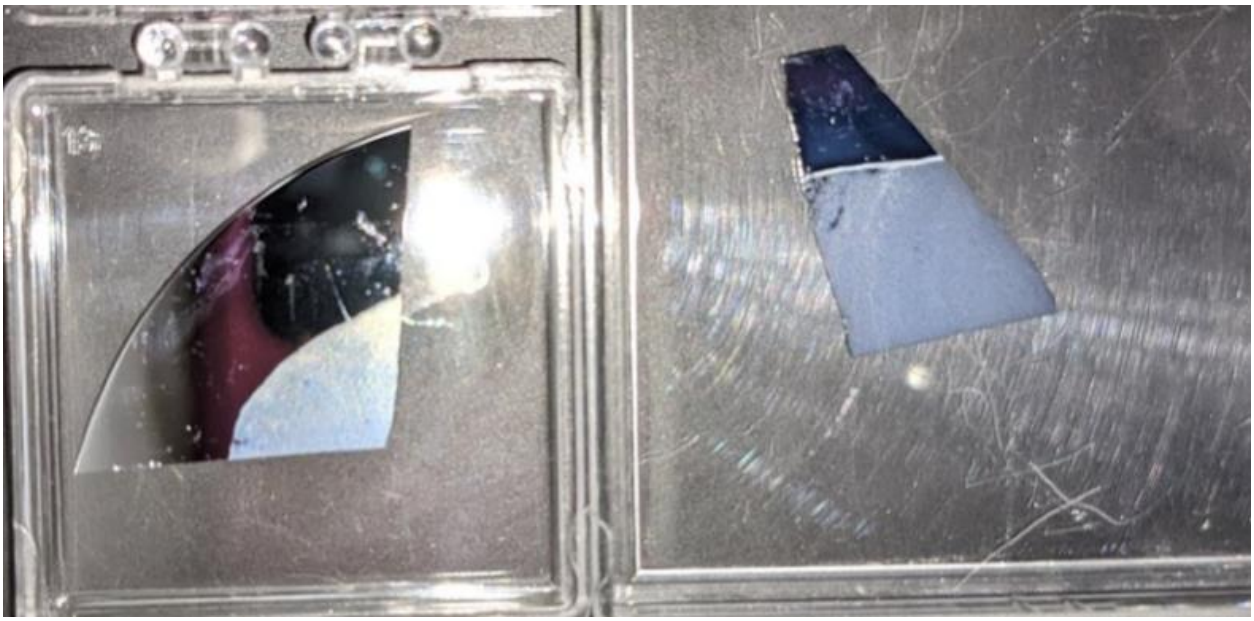

Figure 4.9 Phone image showing the 400nm Supsil sample reflecting light in both the 10 mins and the 40 mins CF4 etch.

The next trial was using the 200nm Sio2 particles, etched with the same etching parameters as before with CF4 etchant gas, giving an anisotropic profile of around 60nm deep structures after 10 mins of etch. From the images in Figure 4.10 and Figure 4.11, the average diameter of the Supsil particles have reduced to almost 100nm size, roughly giving us 10nm/min shrink rate with 22Sccm of CF4. The nanoparticles seemed to be etched into the structures as well; therefore, they cannot be removed as easily with sonication when required for the fabrication step.

4.5.2 Addition of Oxygen Gas for Silicon Dioxide Particle Etching

This setup was followed by another experimental run using an additional etchant gas, oxygen, but in very small concentration at 8scmm mass flow rate. This is fed along with the previous etch recipe, having 22sccm of CF4 at 300W RF power maintaining the internal pressure set point of 350mTorr within the chamber. Care must be taken while handling oxygen plasma separately (not used in this case), as it will heat up the gauge fit internally near the RF supply port of the RIE system. It should be noted that when working with oxygen plasma alone, not as a

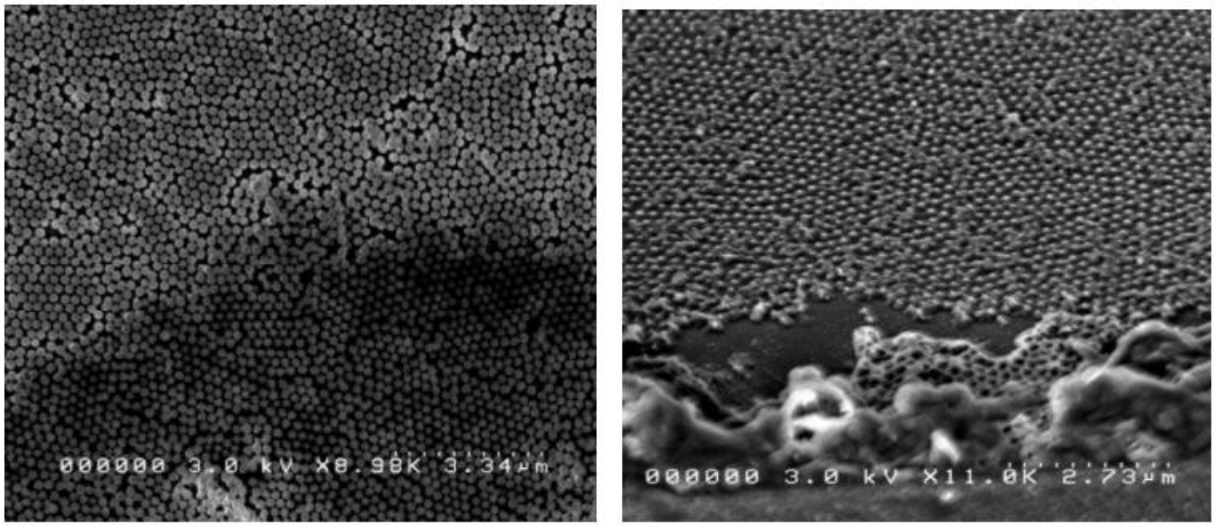

Figure 4.10 The left image shows the top view of 200nm Supsil particle arrangement; right image shows the side view of CF4 etched sample after 10 mins at 11k magnification.

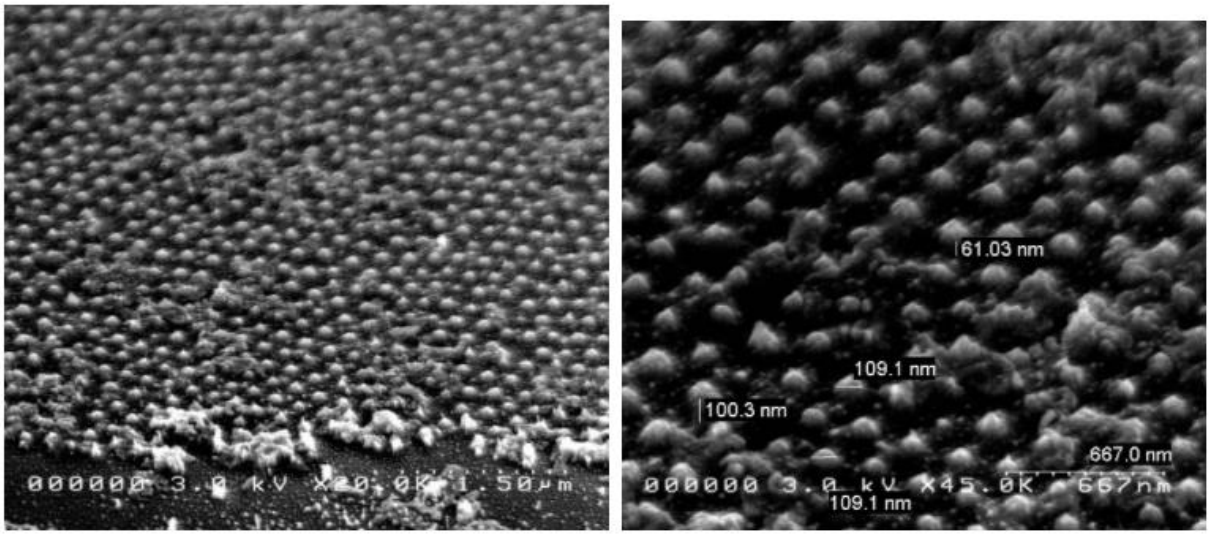

Figure 4.11Both the images show the side view depicting the 200nm nanostructures after 10 mins of CF4 etch at 20kx and 45kx magnification with scales.

mixture with another gas, the RF forward power cannot go beyond 90W, as it will heat up and tear the internal gauge of the end that delivers the power to the plates. This would result in an imbalance while tuning for impedance matching for coupling the supply to the system.

Now, with our setup we ran the desired etch recipe for 10 and 15 mins respectively to visualize around 242- 302nm high nanostructures with the nanoparticle mask layer atop. For the 10 mins etch we can see that the silicon area surrounding the nanoparticles has initiated the process of getting etched when in contact with CF4, as in Figure 4.12. CF4, being less selective to silicon, has started to etch the surface of the substrate, whereas the addition of oxygen has sped up the process of shrinking the particle itself. Therefore, this in addition with CF4 etching has resulted in a transition from cylindrical to more anisotropic moth-eye-like cone structures.

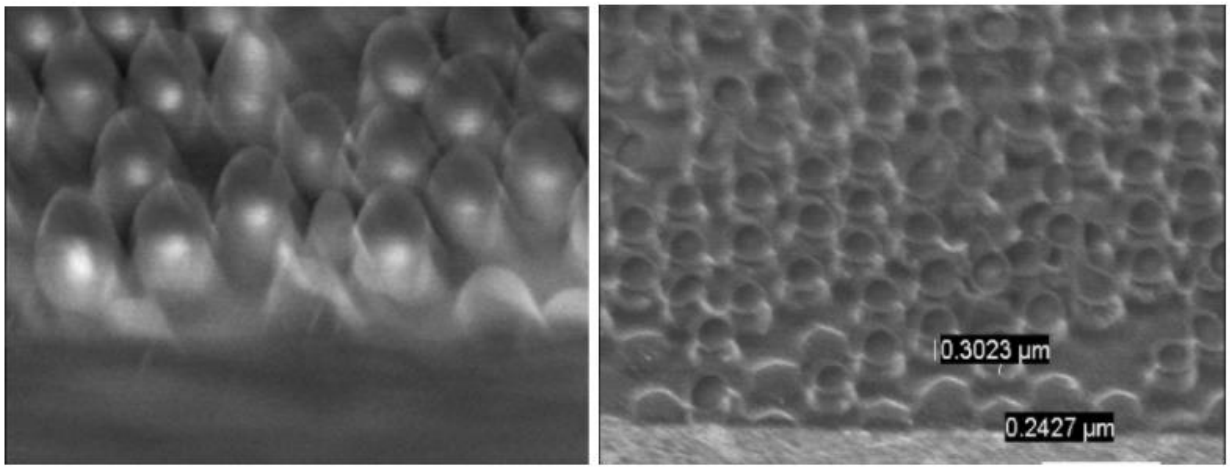

Figure 4.12 SEM image of 400nm particles subjected to 22SSCm of CF4 and 8SCCM of O2 at 300W, after 10 mins and 15 mins, respectively.

The resulting processed substrate was then subjected to mask removal to enable better looking conical structures beneath the underlying oxide layer shown in Figure 4.13. As mentioned earlier, the oxide mask layer can be sonicated with water or etched with buffer oxide etch (BOE) that comprises 1:1 ratio of strong acid hydrofluoric acid with water (H2O). BOE is a wet etchant that can be primarily and extensively used to etch away silicon dioxide mask layer. Subsequently, the results of the then-processed wafer after subjecting to BOE mask removal can be seen in Figure 4.14.

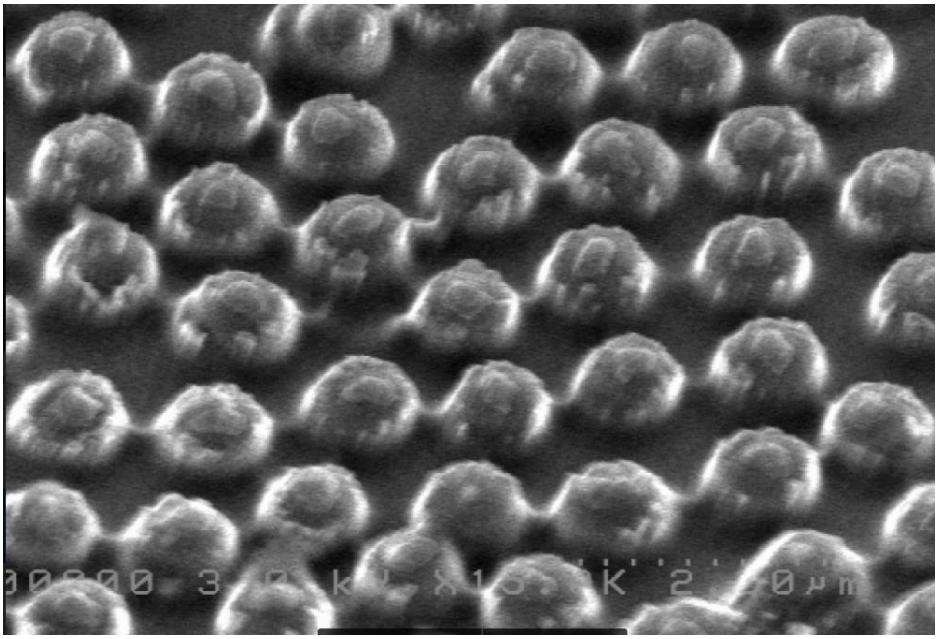

Figure 4.13 SEM image of the Si wafer after 15 mins of RIE and after removing the particles/mask away using buffered oxide etch (BOE) wet etchant.

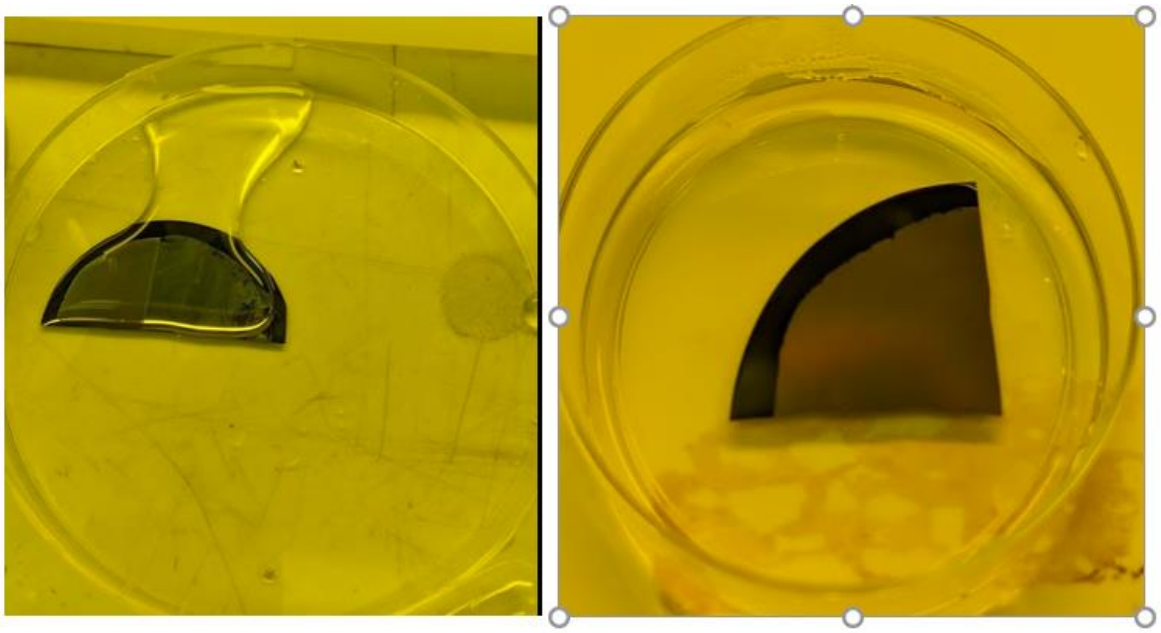

Figure 4.14 Sample showing hydrophilic nature of the nanostructured surface.

4.5.3 Study of etching on NPO-Processed Films.

Previous experiments were done on silicon substrate with silicon dioxide nanosphere mask layer. The introduction of the nanoporous organosilicate films to a silicon surface is done to increase its porosity nature, which would aid in getting deeper structures. Furthermore, NPO films have also been helpful in reducing the refractive index of the surface itself. The preparation and fabrication of these films were explained in detailed in the previous chapter. The processed NPO7735 film would then be used as substrate to deposit polystyrene nanosphere of size 500nm diameter. The preparation and the deposition of the polystyrene can also be referred from the previous chapter. This section enumerates the results and the etch analysis of using polystyrene as the oxide mask layer in forming nanostructures. The sample is then exposed to RIE chamber testing under 300W RF power, with flow rate of CF4 at 22sccm and oxygen at 8sccm.

Polystyrene beads are highly selective to oxygen plasma and shrink in size readily when compared to silicon dioxide particles. The shrinking of polystyrene beads is proportional to exposure towards oxygen. This purpose is helpful in getting small feature sized mask layer, which would eventually aid in producing anisotropic structures of the required diameter.

The shrinking of polystyrene beads with plasma exposure has been previously characterized by Gogel et al, shown in Figure 4.14 .Although for their experiments they had used air plasma, which is a mixture of gases like nitrogen and oxygen, we can still expect a similar trend for how the beads would shrink.

Figure4.16 shows SEM images of the 500nm polystyrene assembly on the NPO films along with the 5 mins of etching with CF4 and O2 plasma recipe provided earlier. The shrinking of the beads was expected giving an average of about 280nm diameter beads, which yields about 40nm per minute when continuously etched, followed by Figure 4.17 showing 170nm deep nanostructures and around 120nm wide particle diameter for 5+3 mins of intermittent etch time. After 5+3+3mins, the polystyrene beads have completely shrunk, and the nanostructures have also been overetched due to overexposure of the plasma. The measurements for each time interval are illustrated in Table 4.1.

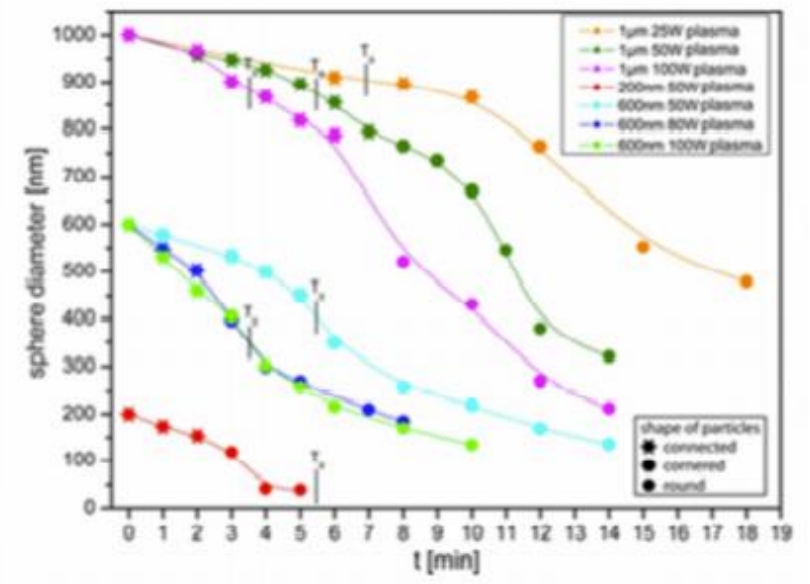

Figure 4.15 Variation observed for polystyrene beads with exposure to oxygen. Source : Gogel et al [18]

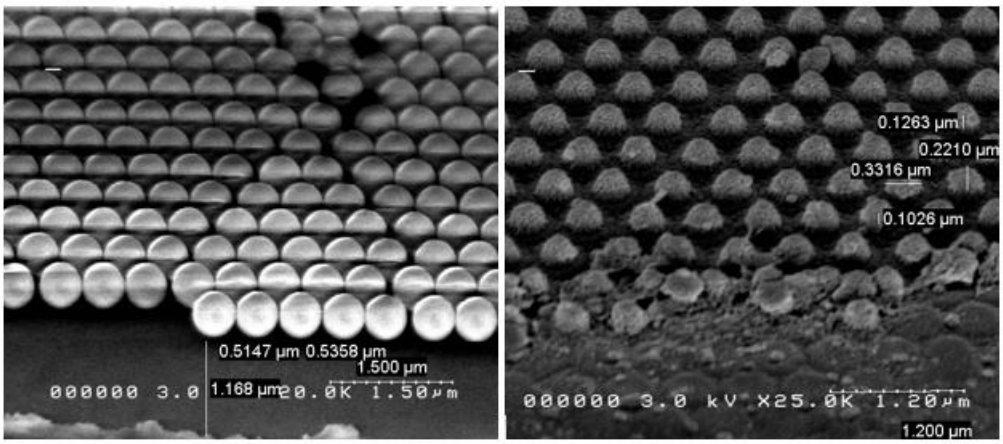

Figure 4.16 (a) NPO 7735 film with 0.5um polystyrene beads (b) after etching for 5 mins.

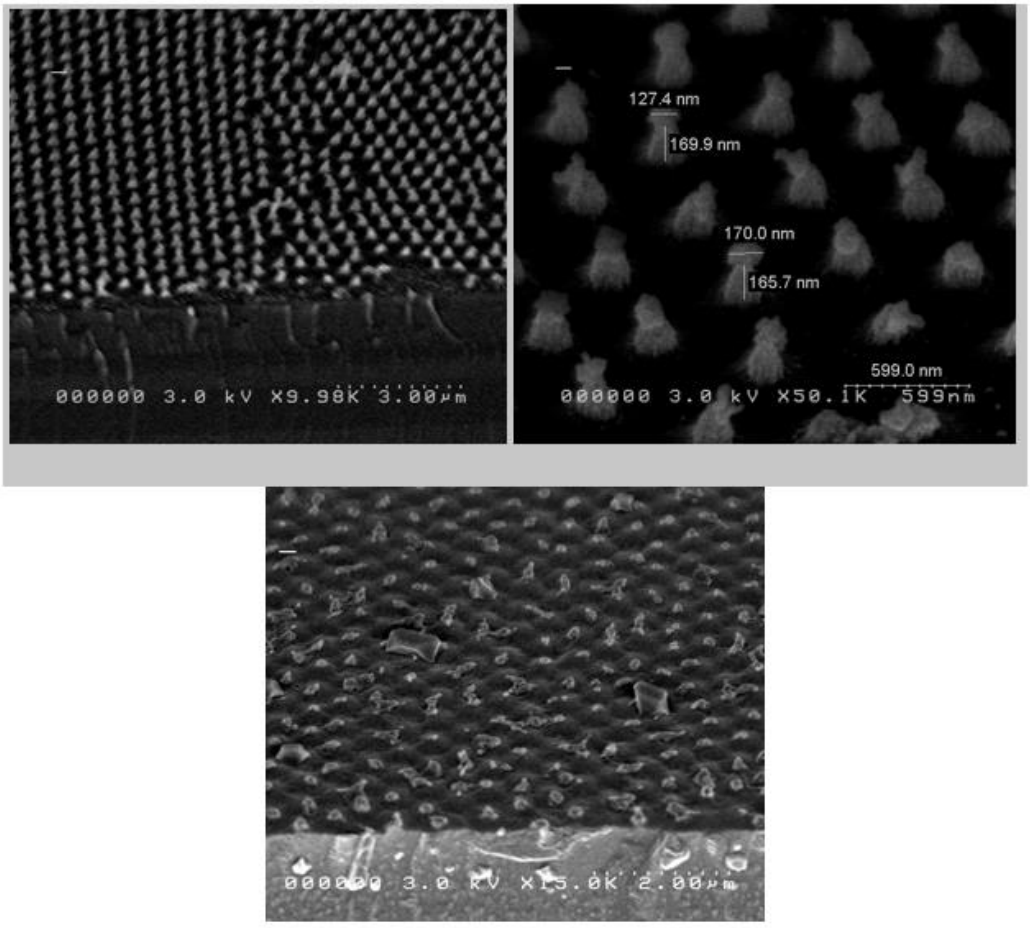

Figure 4.17 NPO 7735 films with 0.5u polystyrene after 5+3 mins with 9.9kx and 50.1kx magnification (c) after 5+3+3 etch time at 15k magnification.

Table 4.1 Polystyrene diameter shrinkage with nanostructure depth on NPO 7735 films for different etch times

RIE plasma exposure time (mins):	**0**	**5**	**5+3**	**5+3+3**
Average diameter (nm)	524.5	276.4	148.7	100.4
Average height (nm)	null	102.6	167.35	195.8

Similarly, for NPO 5573 films, with a different variation with the ratios of the solvent and polymer, this film would give more porous structures, thereby reducing the refractive indices further. The same etch recipe was done for this as well and the SEM images of the 500nm polystyrene assemblies at 0, 5, 5+3, 5+3+3 time intervals are measured and analyzed in Figure 4.18.

The etched structures after 5 mins of etch follows a similar trend as with the NPO 7735. The difference lies in the fact the latter has more collapsed pores, thereby giving a better refractive index of the substrate. After 5+3 mins, it can be seen that the polystyrene has been etched away, leaving tapered-ended nanostructures. The etching rate and analysis are summarized in Table 4.2.

4.5.4 Study of Etching with SF6 Etchant Gas

The initial usage of SF6 as a plasma etchant was discovered by Heineke [19] . After that, it was picked up by Wagner and Brandt to obtain the mass spectra from the etching of Si by SF6.

SF6 is widely known for its highly selective nature for etching properties with silicon and represents an attractive alternate to CF4-O2 plasma etching of silicon and silicon dioxide.

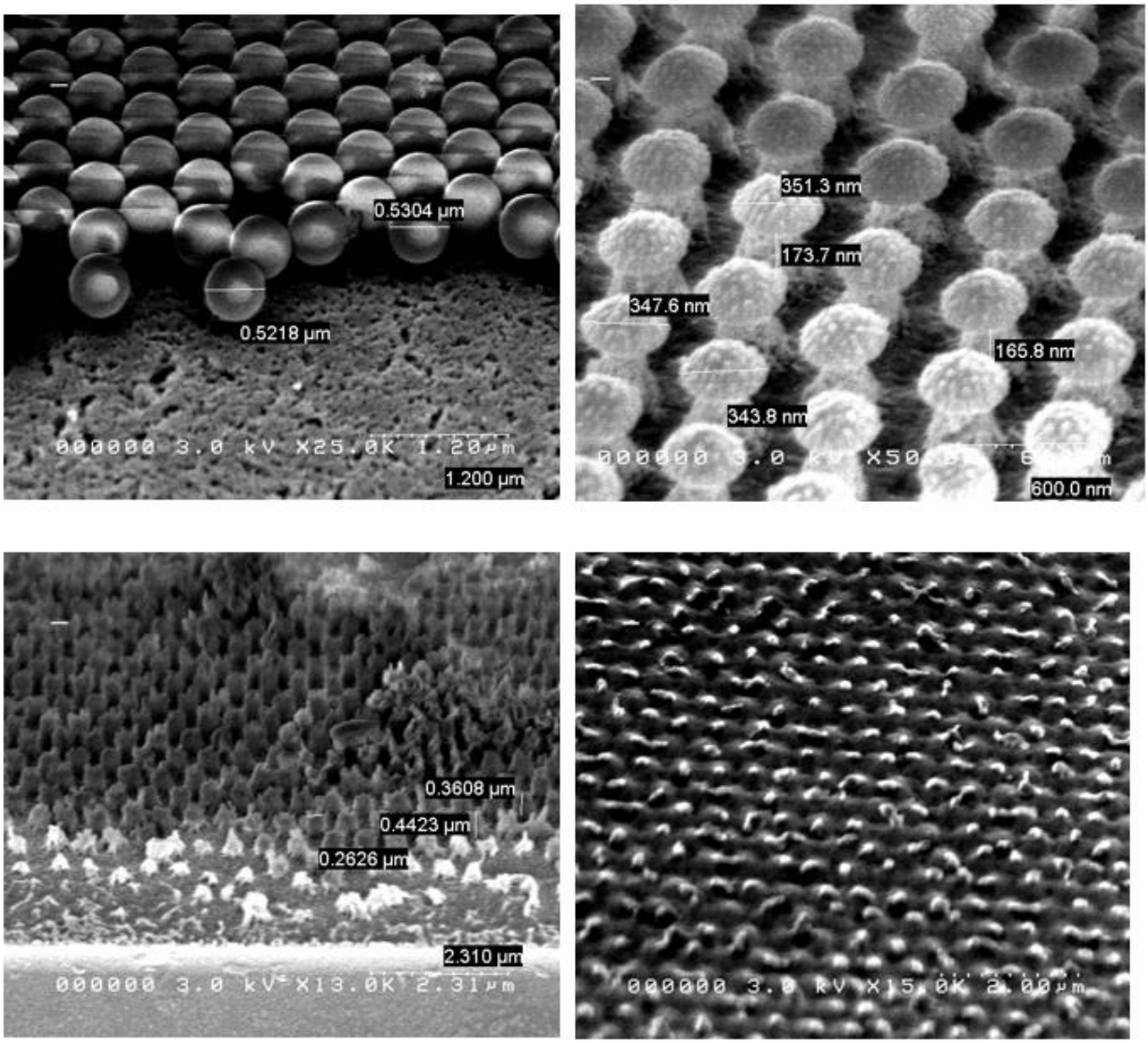

Figure 4.18 NPO 5573 with 0.5um polystyrene beads with 0, 5, 5+3,5+3+3 etch time at different magnifications.

Although the reaction kinetics and products of SF6-O2 is analogous to CF4-O2 plasma, the principal differences lie in SF6 being the dominant cause of dissociative attachment among

electron impact processes, much larger concentrations of atomic fluorine, and the reaction of SF6 to form oxy-fluorides, fluorine, and SiF4 as sole final products.

Table 4.1 Polystyrene diameter shrinkage with nanostructure depth on NPO 5573 film for different etch times.

RIE plasma exposure time (mins):	**0**	**5**	**5+3**	**5+3+3**
Average diameter (nm)	526.1	347.3	null	null
Average height (nm)	null	169.75	355.23	167.8

A procedure explained by Mohammed et al [20], where they experimented with low-power plasma etching using high-density SF6 and low-density oxygen, was carried out. Depending on the oxygen percentage in the mixture, the silicon nanostructures thus obtained were characterized with their etch rate, morphology, and optical reflectance. They were able to find out that with 5% ratio of oxygen in SF6-O2 mixture, a maximum etch rate was observed, as given in Figure 4.19.

There are a couple of differences to point out here. The first and the primary difference is that they used inductively coupled plasma (CCP)-RIE for etching, which would give a higher concentration of electron density, thus plasma, when compared with capacitively coupled plasma (CCP) available at MRDL. Also, the CCP-RIE system has a gas flow controller that can only take a maximum of 100sccm, in contrast to the 200sccm they have used for their recipe. Nevertheless,

their experiments gave us an idea of what to expect when etched with the particular ratio, even with low power.

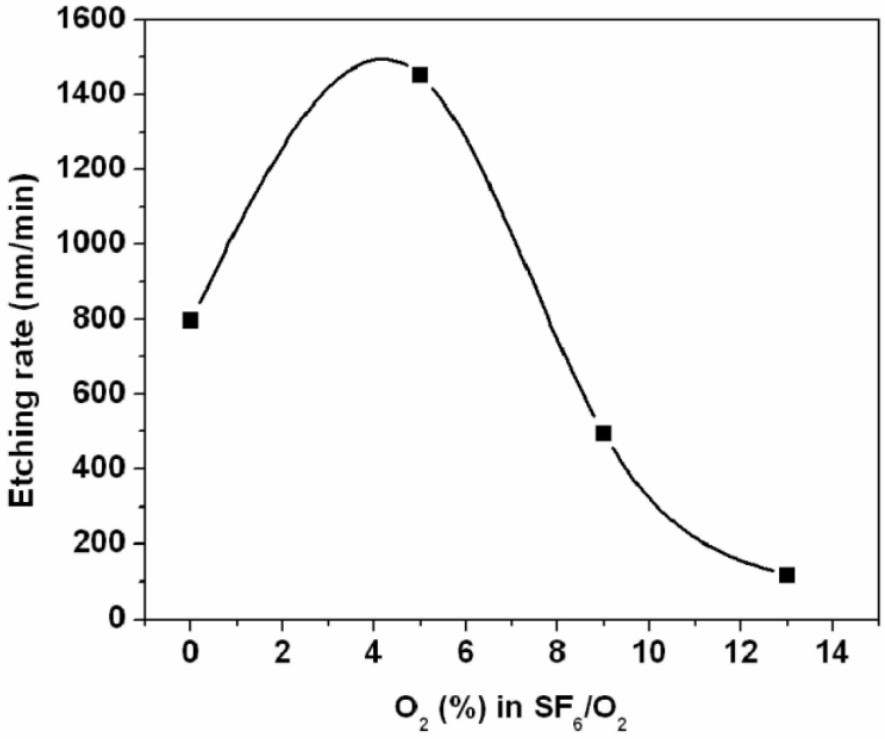

Figure 4.19 Variation of silicon etching rate in SF6/O2 plasma mixture as a function of O2. source :[15].

Our experiments were carried with 200nm feature sized nanoparticles deposited on Silicon substrate. The initial setup using 100 W RF power with 50sccm SF6 and 10sccm O2 along with 450mTorr internal pressure did not yield any growth or etching of the silicon. The SEM images shown in Figure 4.20 are of silicon dioxide nanoparticles with 5, 5+5,5+5+5 minutes of high-density SF6 having 50sccm flow rate with 10sccm oxygen and 200 W RF power with 400mTorr internal pressure. It can be noted here that with the reduction in the RF power, the internal pressure

varies indirectly and thus increases to maintain impedance matching when supplied with RF power as seen in Table 4.3.

Since the SEM image after 5+5 mins in Figure 4.21 was completely overetched, the next step was to etch with the same recipe, but with reduced intervals. It should be noted that there are two ways for etching, one being continuous and the other being intermittent kind of etching.

The difference is with the time, where in intermittent etching, the samples are etched in steps of two 3 mins and continuous having a direct 6 mins etch time. All our experiments are carried out with the intermittent type of etching.

The measured structures with depth and diameter are given in table 4.4, for 3, 3+3 an d3+3+3 mins intervals. A 30nm nanostructure was observed for 3 mins. And as anticipated, 3+3 has yielded 60nm nanostructures, but after 9 mins of intermittent etching, it has completely overetched the sample. This might be due to high power with oxygen that has shrunk the particle completely. As an alternate solution to this, we developed a two-step etch process using polystyrene assemblies.

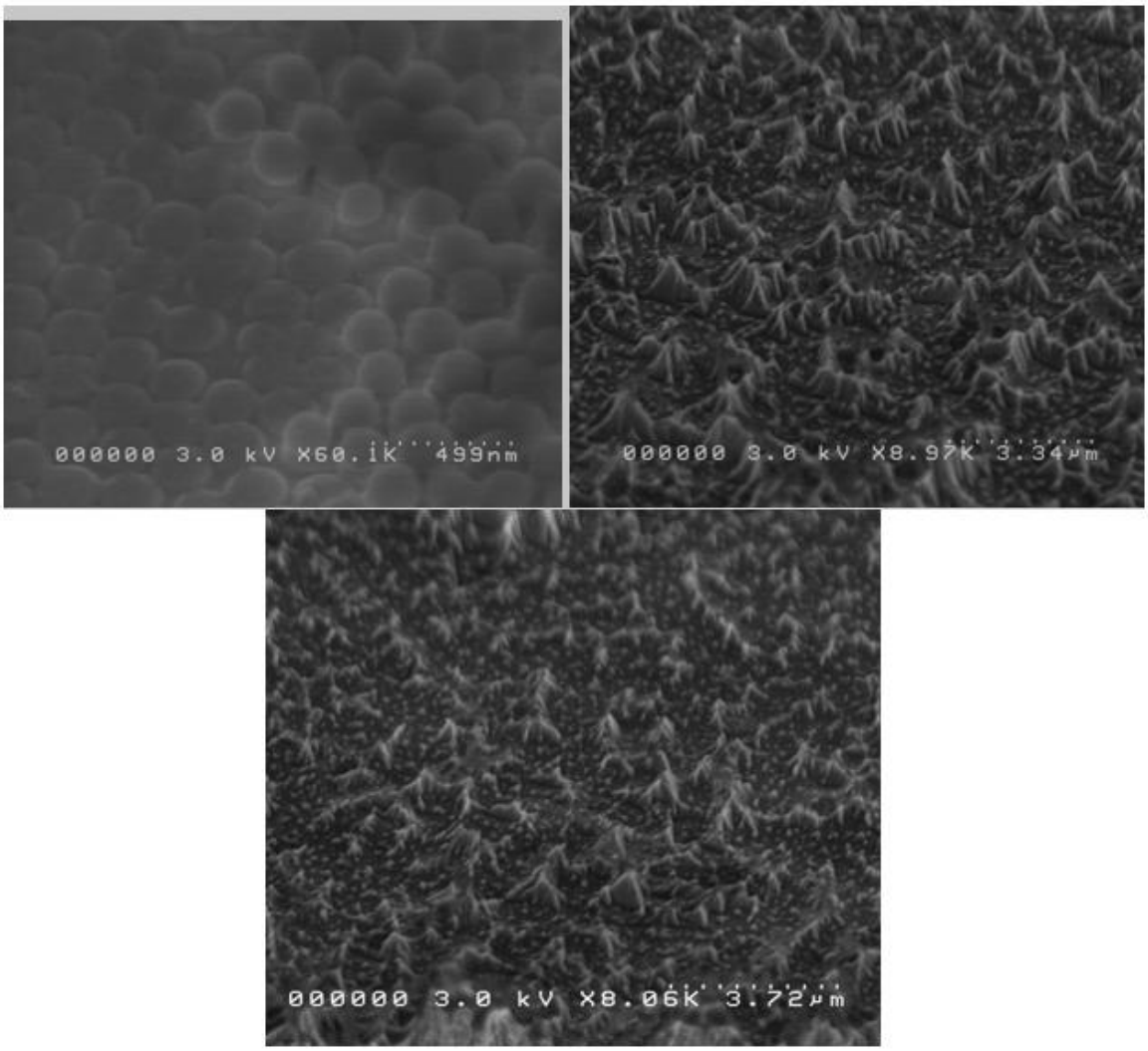

Figure 4.20 Low-power, high-density SF6/O2 etch with SiO2 nanoparticles, with 5, 5+5,5+5+5 mins etching.

Table 4.3 Different etch recipe for high-density, low-power SF6/O2

Sample	SF6 (sccm)	O2 (sccm)	Internal Pr. (mTorr)	Power (Watts)	Etch rate (nm/min)
1.	50	10	450	100	null
2.	50	10	400	200	10

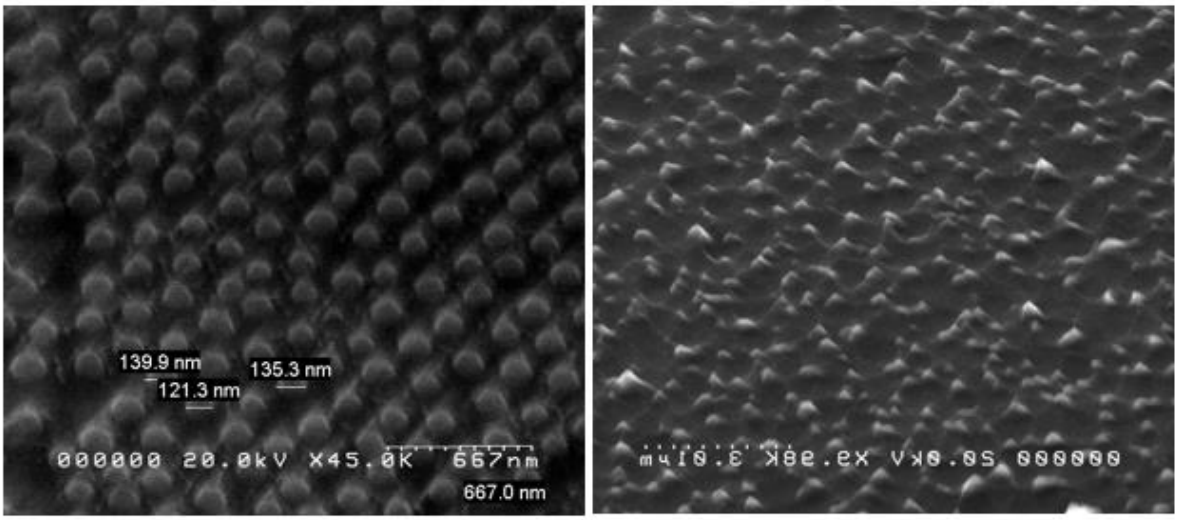

Figure 4.21 Supsil dioxide particles with 200W RF power and high-density SF6/O2 with the left image showing 3 and right image showing 3+3mins.

Table 4.4 Variation of silicon etching with 200W power, SF6/O2 etch

RIE plasma exposure time (mins):	**3**	**3+3**	**3+3+3**
Average diameter (nm)	199.0	135.3	null
Average height (nm)	29.0	61.29	110.22

4.5.6 Study of Two-Step Etch Process:

The step etch process has been developed for low power with higher density plasma concentrations to reduce the level of particle shrinkage, thereby giving rigid nanostructures without

overetching the structures. In the two-step process, the first step includes shrinking the particle with oxygen plasma. The second step includes etching anisotropically with lower density SF6/O2 concentrations. As the shrinkage behavior of polystyrene is what we can control more of, we will be dealing with polystyrene particles of size 500nm and shrinking to about 200nm and then etching anisotropically with the second step.

Figure 4.22 depicts the polystyrene assembly pictures taken at the first step of the etch process. For the etch recipe, we went with 30sccm of oxygen at 90W RF power and 450 mTorr internal pressure. As to be expected, the polystyrene beads have shrunk into each other with an etch rate of approximately 100nm per minute. These samples act as our controls for next step of the two-step etch process. Table 4.5 provides the kinds of samples we will be etching with their respective etching intervals for a better understanding.

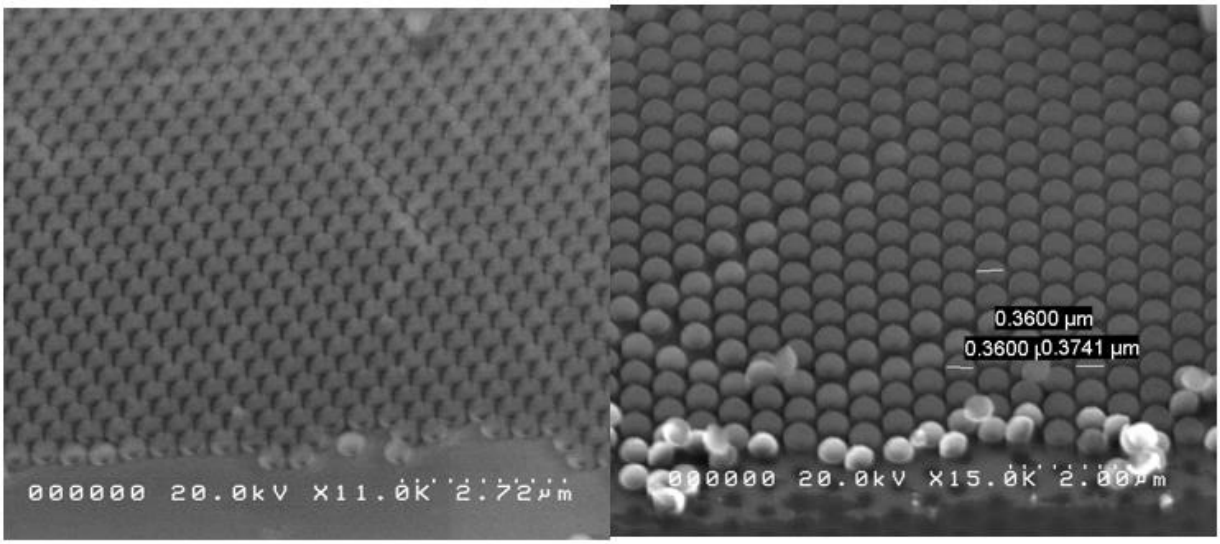

Figure 4.22 Polystyrene shrinkage with oxygen plasma with 3minsetch on the left and 3+3mins etch time on the right

Table 4.5 Sample kinds with their respective etching intervals used

Sample	**A**	**B**	**C**
30scccm O2_90WRFsupply_Time(mins)	3	6	3
50sccm SF6/8sccm O2_200WRFsupply_time intervals run for (mins)	3+3	3+3	3+1+1+1

4.5.6.1 Sample A : Oxygen- 3mins etched results :

Figure[4.23] is the end result of the polystyrene beads shrunk and the silicon getting etched with 22sccm of SF6 and 8 sccm O2 gas mixture at 200W and 450mTorr internal pressure set point.

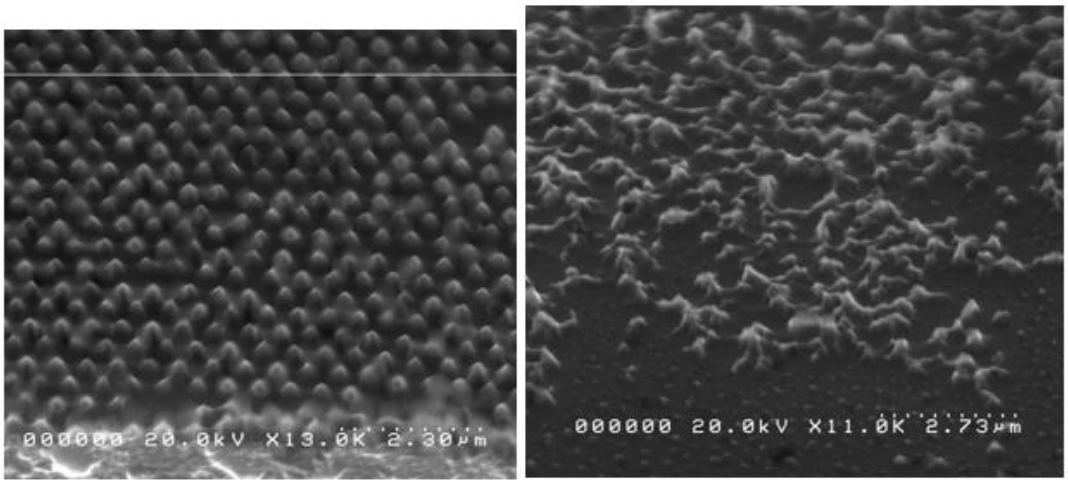

Figure 4.23 Sample A when subjected to 3 mins as shown on the left and 6 mins of SF6/O2 etch process as shown on the right.

In Figure 4.23, named Sample A, the etching of silicon has initiated, but after 6 mins of etching, it has overetched the surface, resulting in blunt, tapered structures. This is because the

etch recipe includes oxygen, which has shrunk the polystyrene beads at a faster rate compared to SF6 etching with silicon.

4.5.6.1 Sample B Oxygen: 6 Minutes Etched Results

Now in Figure 4.24, we can see the nanostructures desired, having an average of 200nm deep silicon nanostructures that can be seen in Figure 4.24b. The 6 mins of polystyrene shrinkage has given us the required feature size of the mask layer, resulting in conical moth-eyed structures. As expected, 6 mins of SF6/O2 etch in Figure 4.25 has overetched the sample because of faster shrinking of the polystyrene beads. Thus, as the next step to this trial was run, the result for the intermediate time intervals in between the etched and the overetched has to be analyzed, that is 3+1 to 3+1+1+1 to see if the results would be helpful.

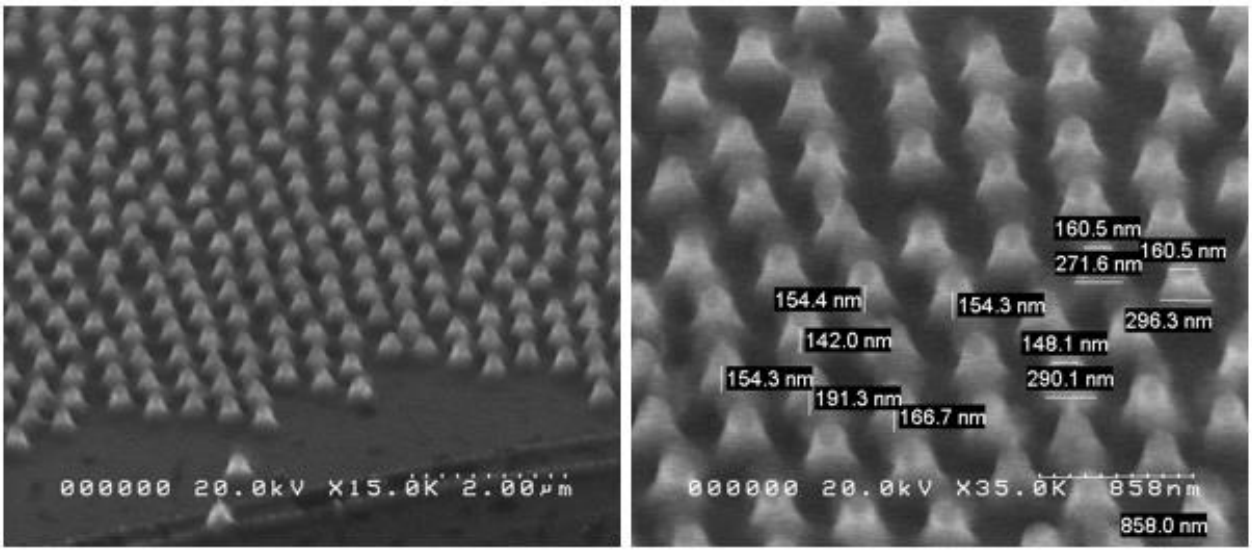

Figure 4.24 The left image shows Sample B with 3 mins etch with 15k and right with 35k magnification.

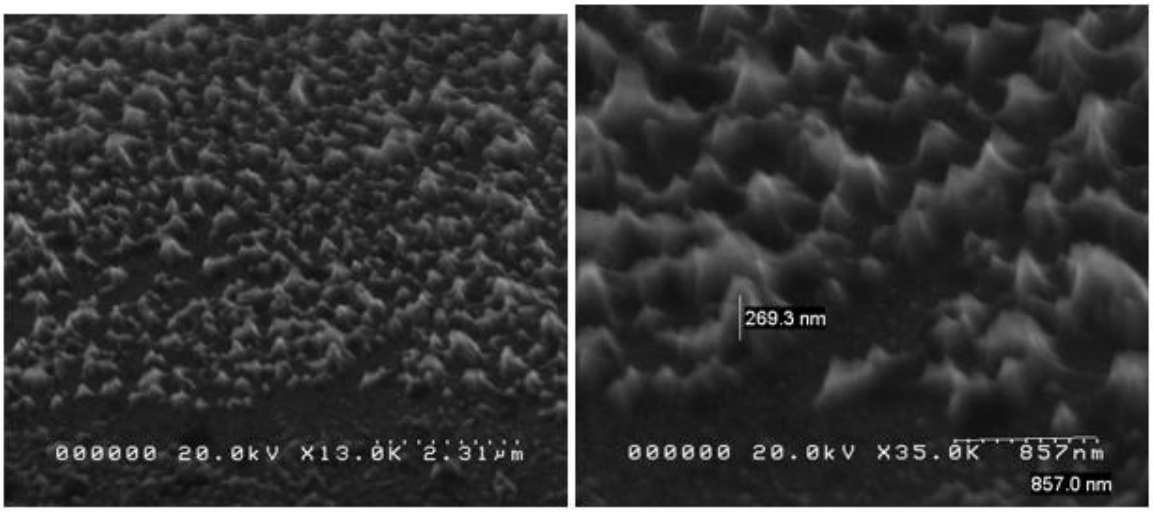

Figure 4.25 Sample B with 6mins of SF6/O2 etch at 13k and 35k magnification as shown on the left and right respectively.

4.5.6.2Sample C Oxygen: 6 Minutes Etching with Modified Intervals

With the modified intervals to the above etch recipe, we see that because of etching the samples as continuously for 3 mins like in Sample B, we have gone with steps of 1 mins increments for a total of 6 mins by running for 3+1, followed by 3+1+1 and finally 3+1+1.

In 3+1 found in Figure 4.25, the nanostructures can be seen as though the nanoparticle oxide layer had started to shrink faster and resulted in tapered ends. For the 3+1+1 sample as well, in Figure 4.26c, the polystyrene has shrunk further, forming tipped-conical structures. It can be noted that the etch results for continuous 3+3 in figure 4.26b and the intermittent 3+1+1+1 Figure 4.26d can bring about a vital importance, as in the former it yielded overetched results. The latter still has distinctive structures, but it can be also noted that the polystyrene has completely shrunk into the structures itself.

From all the analyzed results, sample C in Figure 4.26 with 6 mins O2 etch and 3 mins of SF6/O2 etch had better desired conical and parabolic structure, with an average of 161.5nm deep structures and having around 289 nm lateral spacing between them. This will be the sample used for our forthcoming experiments.

4.5 Mask Removal

After etching the substrate by using oxide layer as a mask for etching, it is then required to remove the oxide particles using buffer oxide etch (BOE) to remove the oxide layer, thus exposing the substrates having tapered nanostructures at the top. The entire fabrication steps enumerated above are illustrated with the schematic shown below in Figure 4.27. Here, you have the plasma exposure step as discussed in the second chapter to remove any impurities from the silicon substrate surface and increasing the hydrophobic nature for enhanced self-assembly technique enabled deposition. This is followed by the deposition of the colloidal particles, followed by etching the silicon substrate to get nanostructures. Finally, the colloidal mask layer is laid off using wet etchant such as buffer oxide etch or sonication with ethanol to expose the conical nanostructures underneath.

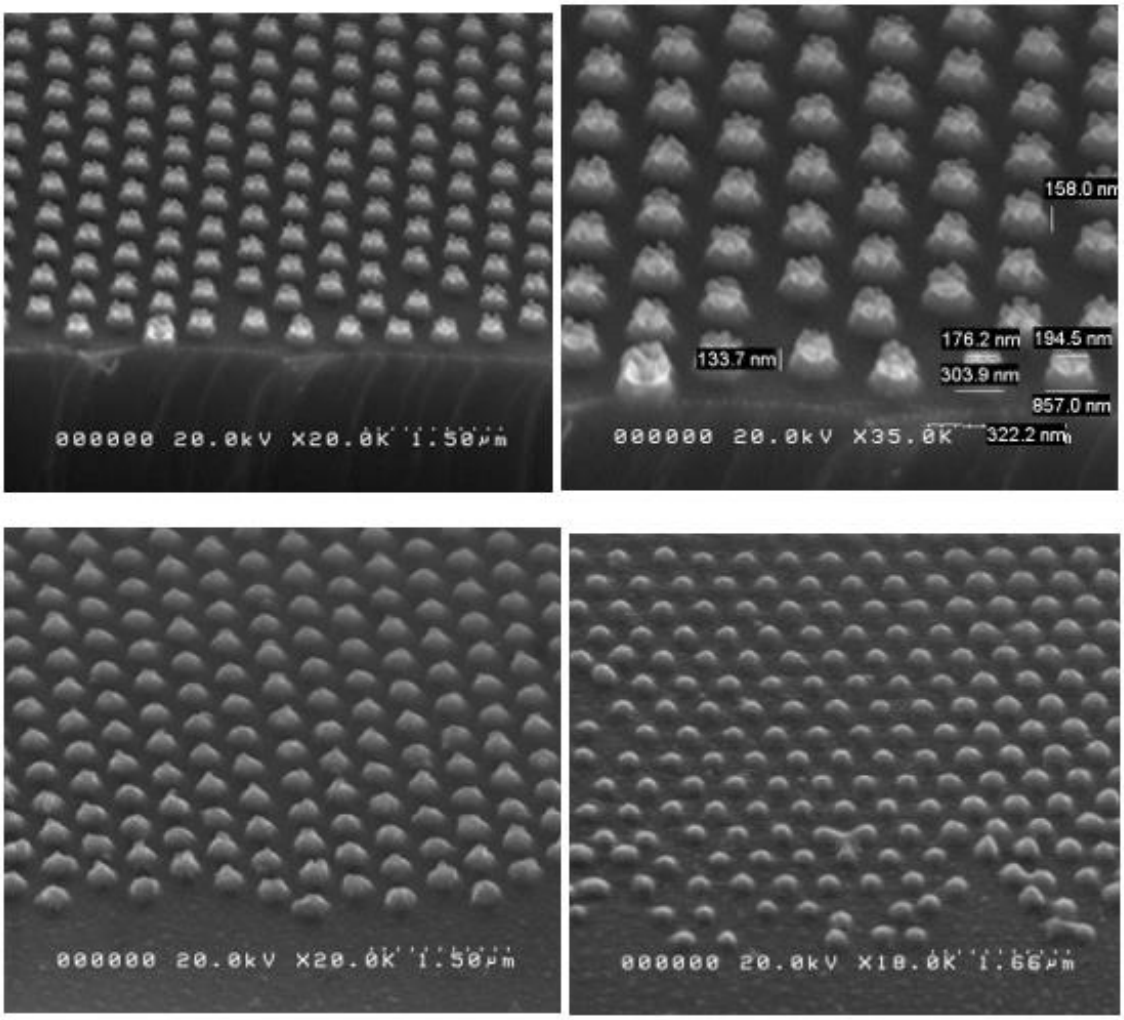

Figure 4.26 Sample C with 6mins o2 and SF6/O2 etch study for (a) 3+1 mins at 20k and (b) 3+1 mins at 30k magnification (c) for 3+1+1 mins and finally (d) 3+1+1+1 mins.

After getting the desired 200nm deep anisotropic nanostructures, the Figure 4.28 gives the result of the conical nanostructures that was underneath the oxide mask layer, without the oxide polystyrene particles on top. These obtained structures on the silicon substrate will be used as a master structure for large-scale replicating techniques addressed in the next chapter.

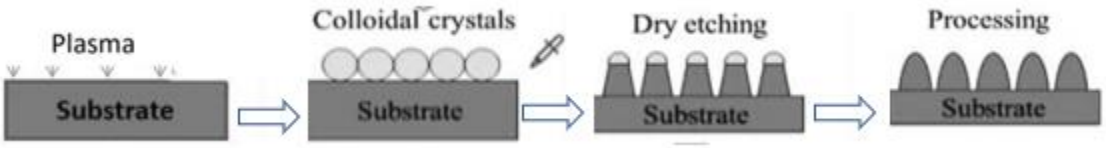

Figure 4.27 Fabrication schematic for the above completed process.

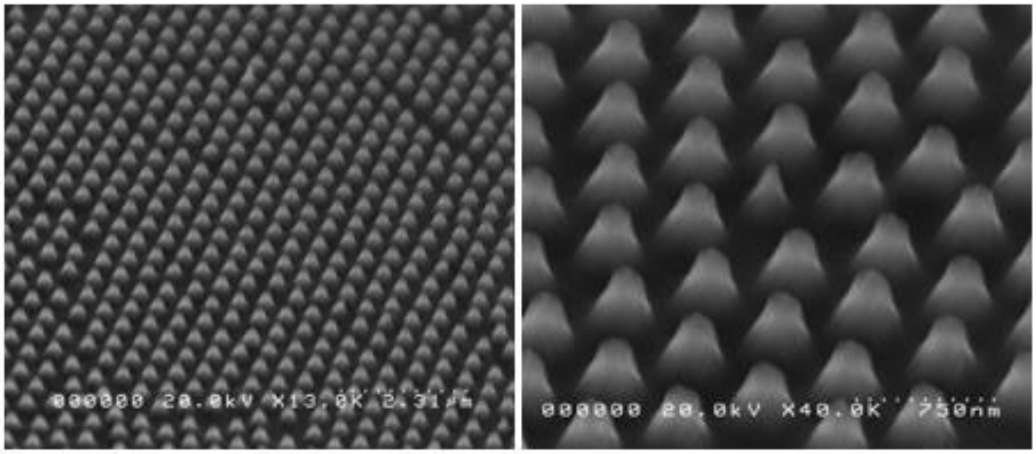

Figure 4.28 Exposed conical structures after mask removal.

5. NANOIMPRINT LITHOGRAPHY

With the silicon substrate etched with nanostructures of 200nm deep, we now move on with the next goal for this research; large-area replication of the nanostructures . The conventional method of fabrication, although fabricated with cheap and rapid techniques, is not practical when it comes to larger areas. Using current patterning methods, mass producing large-area nanostructures, especially nanopatterning on various curved or non-flat surfaces, fragile substrates, or flexible substrates, is particularly difficult. Furthermore, various current micro/nano-manufacturing technologies, such as optical lithography, electron beam lithography, centered ion beam lithography, interference lithography, and so on, are unable to meet any of the practical requirements of industrial-scale applications in terms of high resolution, high-throughput, low cost, large-area patterning, and so on [21] . Hence, the purpose of this chapter is to develop a process that can be done to allow the formation of a particular pattern and then replicate it over a large area. The factors that determine the best method should have a quality or a high throughput replication tendency and also be easily adapted with less-expensive materials. For this reason, large-area nanoimprint lithography (NIL) has been regarded as one of the most promising micro- and nano- manufacturing technologies for mass production [21]. This opens the door and paves the way for a wide range of commercial applications that were previously unimagined or unfeasible.

Recent years have seen significant advancements in large-area nanoimprint lithography. This chapter primarily provides an overview of recent developments in large-area NIL processes.

We take advantage of fabricating a replica molding, particularly a master replica mask. These master molds can be made from pre-existing molds like DVDs with 800nm groove size, or they can be fabricated using any of the etching processes entailed in the previous chapter. Once they are molded to the master structures, the elastomer is cured and peeled away, creating a polymer stamp which is used to transfer a particular pattern over a surface area. This chapter enumerates the processes and technique used for large-scale development. Finally, prospects, challenges, and potential directions for large-area NIL on an industrial scale are discussed. A large-area nanoimprint lithography infrastructure is proposed.

5.1 Sacrificial Layer Mediated Nanoimprinting (SLAN)

In a multiscale fabrication developed by Raut et al. [4], they have described their invention in fabricating large-area substrates using a simple and a scalable technique by a distinctive approach called sacrificial layer mediated nanoimprinting (SLAN). As their initial step, the moth-eye AR nanostructures were first created by imprinting the appropriate mold onto a polycarbonate film (PC). The nanostructures were 200 nm in diameter and height, and they were arranged in a hexagonal close-packed (hcp) pattern, similar to the AR nanostructures found in biological moths. The imprinted surface was then spin coated with a 20 wt.% solution of poly(sodium 4-styrenesulfonate) (PSS) to form a 500 nm thin film (Figure 5.1b). At a temperature higher than the glass transition temperature of PC, a second imprinting of the microlens arrays was performed on the nanostructured patterns encapsulated in the PSS thin film [4].

The in-between PSS layer prevented the underlying AR nanostructures from buckling or deforming while the second imprinting was taking place and the nanostructured surface was being formed into microlens arrays. PSS does not turn into a molten state and is able to firmly protect

the AR nanostructures since its melting temperature (Tm) is 450 C, which is much higher than that of PC (Tm = 155 C). The imprinted substrate was submerged in water after mold release, resulting in complete dissolution of PSS from the imprinted surface, as shown below in Figure 5.1. This technique takes advantage of PSS and polycarbonate's preferential solubility in polar and nonpolar solvents, respectively. Highly uniform multiscale ommatidial arrays containing microlenses were developed, and the tops were covered with AR nanostructure patterns.

Although using a large mold is the simplest way to produce large-area nanostructures, it would still require high and uniform pressure that ensures the structures are being transferred completely, without any deformations or damage to the mold. Therefore, in achieving promising results, we will have to consider three critical issues: 1) achieving uniform distribution across the full wafer, 2) ensuring fully conformal contact on the imprinting full field, and 3) preventing trapped air bubble defects. Therefore, the proposed technique in the next section demonstrates possible solutions to the issues faced.

5.2 PDMS-Molded CD Gratings

The elastomeric mold that is going to be used in our experiments will be carried out using polydimethylsiloxane (PDMS). This can be produced by preparing a 1:5 ratio of the crosslinker to the base and mixing it continuously. This is followed by pouring it over our master structures to cover the entire surface with a thickness of atleast 2mm to ensure easy removal during lift off. It is then allowed to cure overnight, following which the mold is cut and peeled off carefully using a blade. For fabricating these stamps, we will be using PMSSQ ink. The next paragraph entails the purpose of using PMSSQ in our research work.

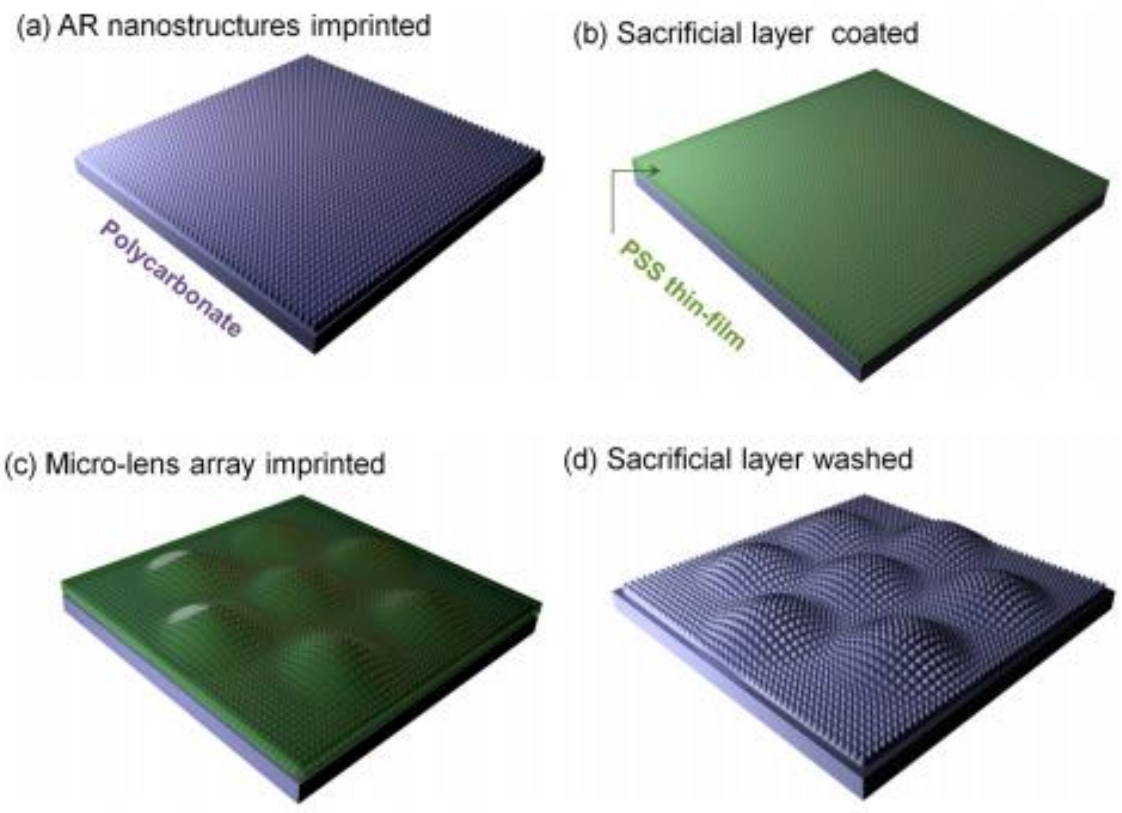

Figure 5.1 SLAN fabrication steps as developed by Raut et al. [4].

The use of polymethylsilsesquioxane (PMSSQ) nanoparticles dispersed in polypropylene glycol (PPG) is what we would like to study at the moment. It is the most studied starting material for nanoporous dielectrics [15]. This along with being an inexpensive material makes it suitable and compatible for preparing the replicating master structures. PMSSQ-based films are naturally hydrophobic, thus minimizing degradation due to moisture absorption. The idea is to fabricate nanoporous films and etch them to get anisotropic structures. These would act as our master molds for replication. PMSSQ is further utilized as a nanotransfer ink in getting replicating structures with high throughput. It is a highly temperature-stable glass resin and is used as the primary component of our nanotransfer ink. The resulting nanotransferred structures would have a high temperature stability owing to the strong Si-O-Si formed with the PMSSQ chain as shown in

Figure 5.2 . It could be made to retain the printed shape even after subjecting the structure to temperatures as high as 550 °C. All these points make it advantageous for us to employ the usage of PMSSQ ink for our experiments pertaining to stamping from here on.

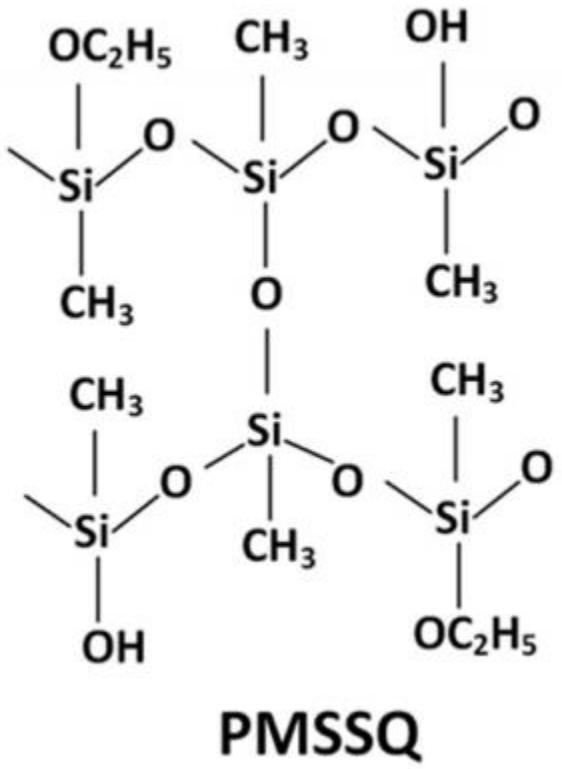

Figure 5.2 PMSSQ chemical configuration. Source: [14].

A 3% solution of PMSSQ is made in 10ml of ethanol or propylene glycol methyl ether acetate (PGMEA) along with 25ul of aminopropyl triethoxy silane (APTES) added as a crosslinker in order to facilitate cross linking of the film.

As shown in the Figure 5.3, stamps were made by spin coating the solution over a elastomeric mold, or the PDMS mold in our case, and brought in contact with the substrate to get a conformal contact. If the contact is still not tight and even, a slight pressure can be applied to the stamp for proper adhesion to the substrate. It is then baked at 75 degrees Celsius for 2 mins to allow proper bonding to the substrate before peeling it away. Figure 5.4 shows the HD-DVD grating stamp on the substrate. Notice how the colorful pattern seen on the DVD can be seen on the stamp printed on the substrate.

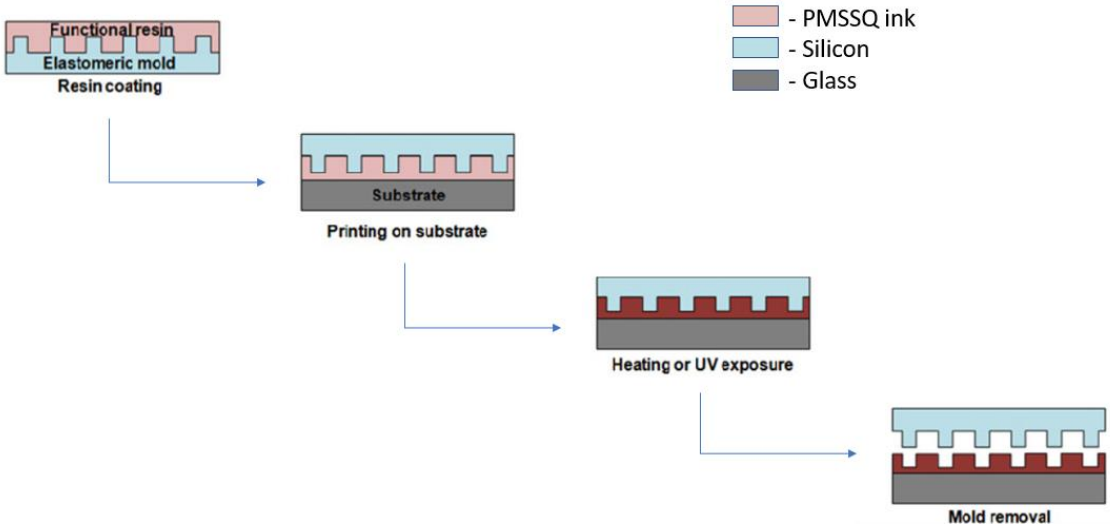

Figure 5.3 Schematic diagram of PDMS mold preparation

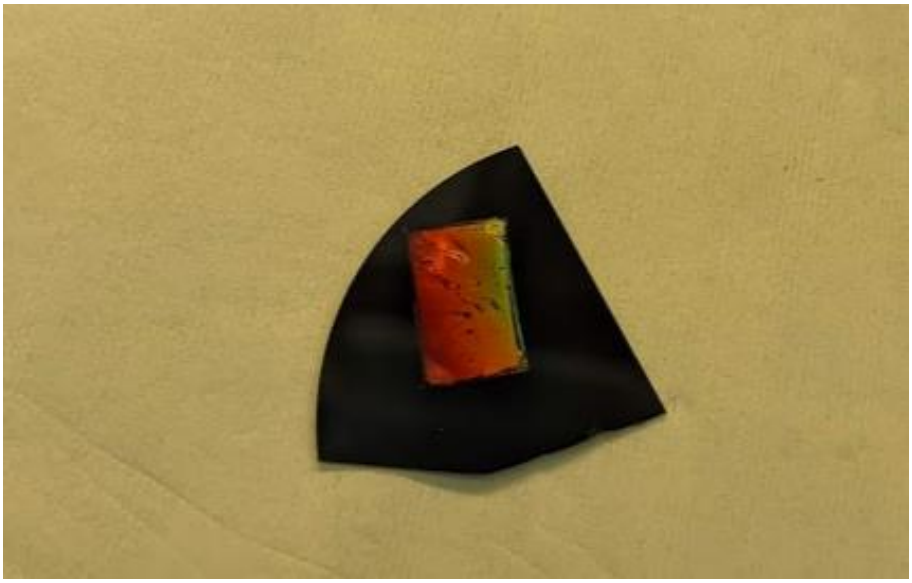

Figure 5.4 HD-DVD grating stamped on silicon substrate using PDMS mold and PMSSQ ink.

6. SIMULATION STUDY

6.1 Simulation Setup

The above fabrication can be done virtually with the help of Lumerical Software. It uses the finite-difference time-domain (FDTD) algorithm, which is considered the gold standard to enable designers to accurately model components for photonic simulations. For this research, the simulating setup is created as shown below in Figures 6.1 and 6.2 to get the moth-eye structures on a silicon substrate. To know how much power the moth eye structure absorbs, two frequency-domain power monitors are used: R measures the total reflection behind the source and T sensor is mounted on the moth-eye interface and the substratum to measure the power in the substratum.

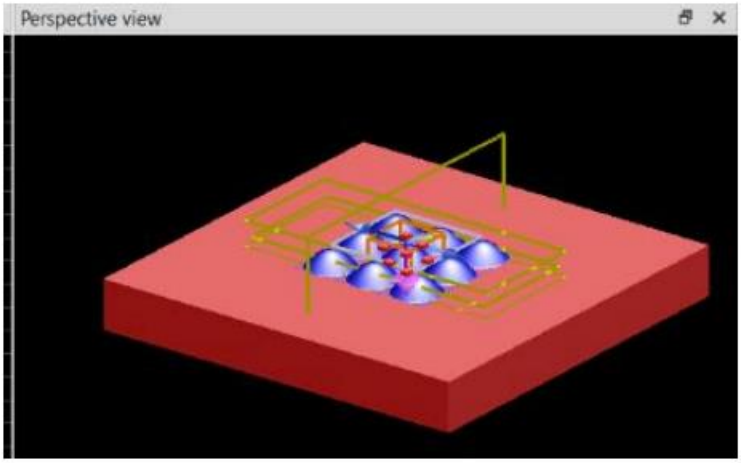

Figure 6.1 Simulated moth-eye structures using Lumerical.

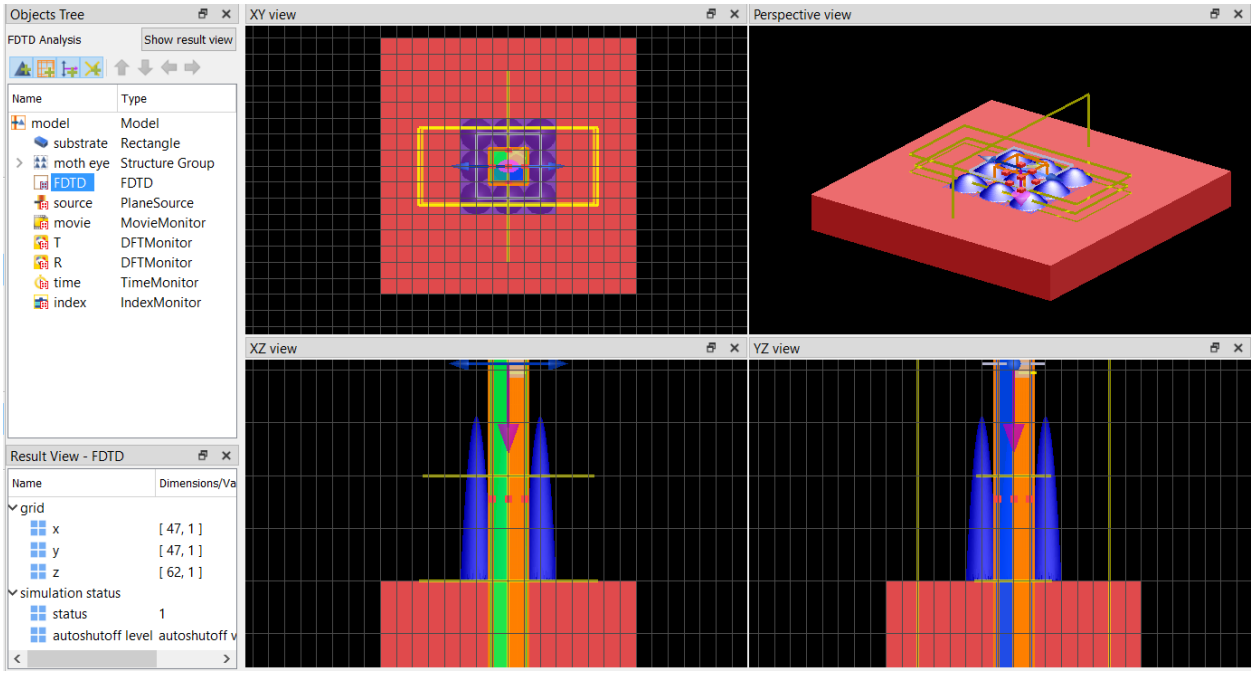

Figure6.2 Lumerical design setup of the nipple-arrayed moth-eye structures.

6.2 Results and Discussion:

The above experiment is simulated using Lumerical FDTD for wavelength ranging from 350nm to 800nm. The simulation was run for different substrates and PMSSQ moth-eye structures (refractive index 1.35). It was carried out with different radius of curvature and pitch size.

6.2.1 Si Substrate with PMSSQ Moth-Eye Structures, Radius of Curvature = 100nm, Pitch = 500nm.

Figure 6.3a shows the normalized power of absorption by the substrate, moth-eye structures and the amount of reflection versus wavelength. Figure 6.3b shows the amount of total absorbed power by the substrate and moth-eye structures across the wavelength.

Figure 6.4 depicts the intensity (|E|^2) profile plots at the minimum and maximum wavelengths as well as the center wavelength. From the plot, we can see that for 350nm to 850nm

wavelengths, the absorption by the moth-eye structures is less and that by the substrate is high. Hence, for the next simulation we used silicon dioxide substrate for experimental purposes.

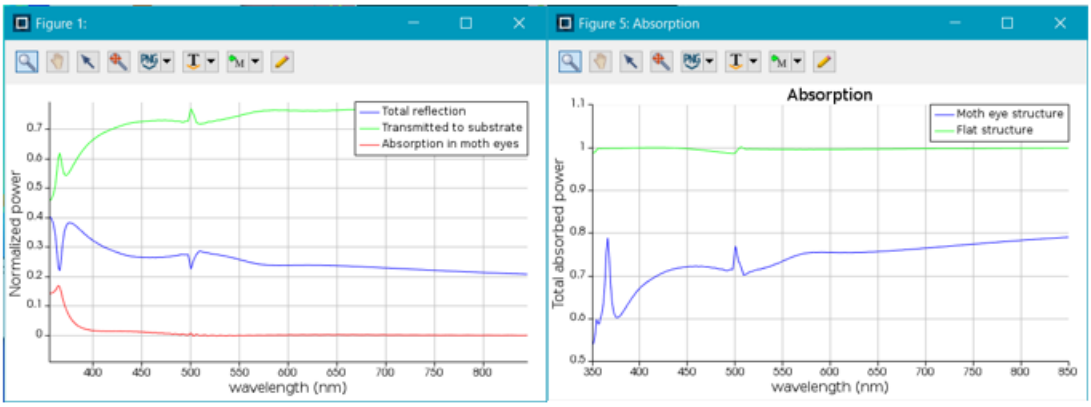

Figure 6.3 (a) Normalized power and (b) absorption power absorption graph for Si substrates with PMSSQ moth-eye structure for radius of 100nm and pitch size of 500nm.

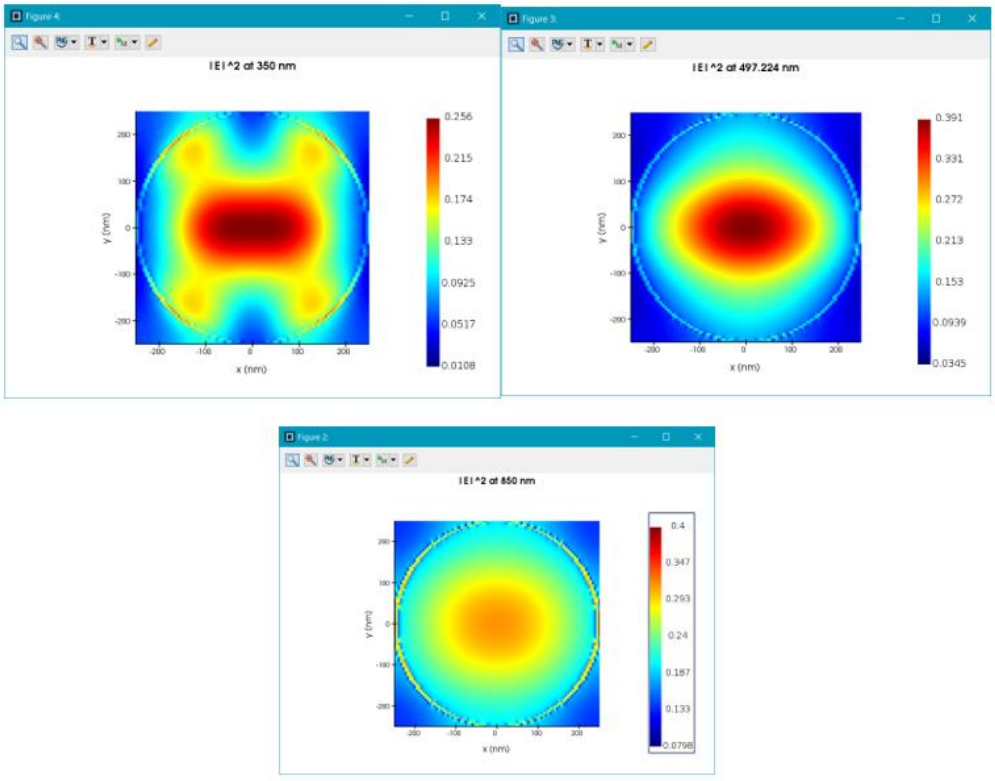

Figure 6.4 Intensity (|E|^2) profile plots at the minimum, maximum and center wavelengths.

6.2.2 Glass (SiO2) Substrate and PMSSQ Moth Eye Structures, Radius of Curvature = 100nm, Pitch = 500nm.

After changing to a glass substrate, maximum transmission in the substrate can be visualized, along with zero absorption by the moth-eye structures and zero total reflection (Figure 6.5). However, the total absorbed power is less for wavelengths below 500nm and remains almost the same for wavelengths above 500nm. It can also be seen that the total absorbed power for both the substrate and the moth-eye structures are overlapping and the same. While coming to the intensity plots, it seems like they are pixelated (Figure 6.6), which I thought would be because of mesh settings at first, but this design is not simulated using mesh setting.

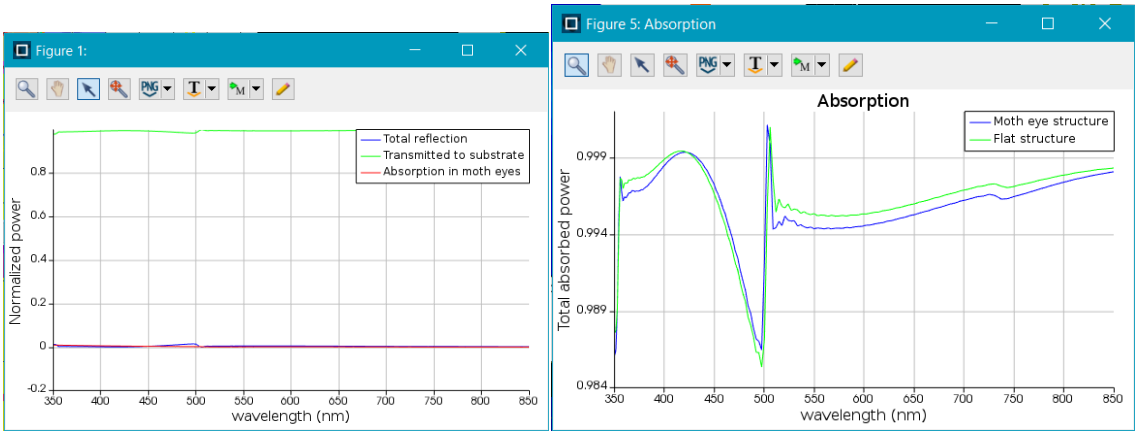

Figure 6.5 (a) normalized power and (b) absorption power absorption graph for SiO2 substrates with PMSSQ moth-eyed structure for radius of 100nm and pitch size of 500nm.

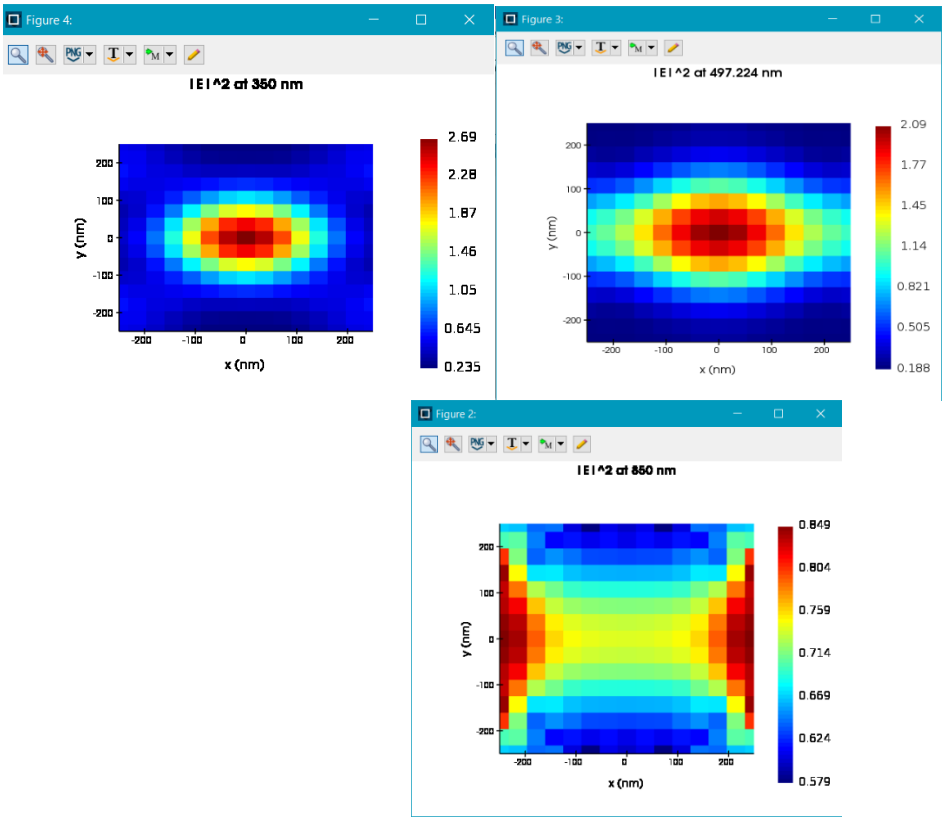

Figure 6.6 Intensity (|E|^2) profile plots at the minimum, maximum and center wavelengths

6.2.3 Glass (SiO2) Substrate and PMSSQ Moth-eye Structures, Radius of Curvature = 100nm, Pitch = 505nm.

For this simulation, the same normalized power results can be seen for this design setup as well (Figure 6.7). There is small gradual decrease in the total absorbed power for the moth-eye structures (Figure 6.8).

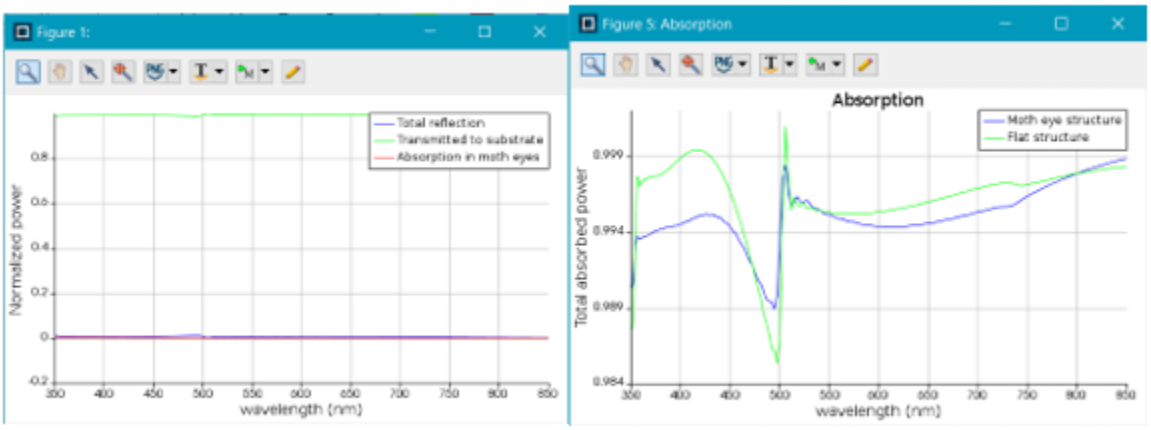

Figure 6.7 (a) normalized power and (b) absorption power absorption graph for SiO2 substrates with PMSSQ moth-eyed structure for radius of 100nm and pitch size of 505nm.

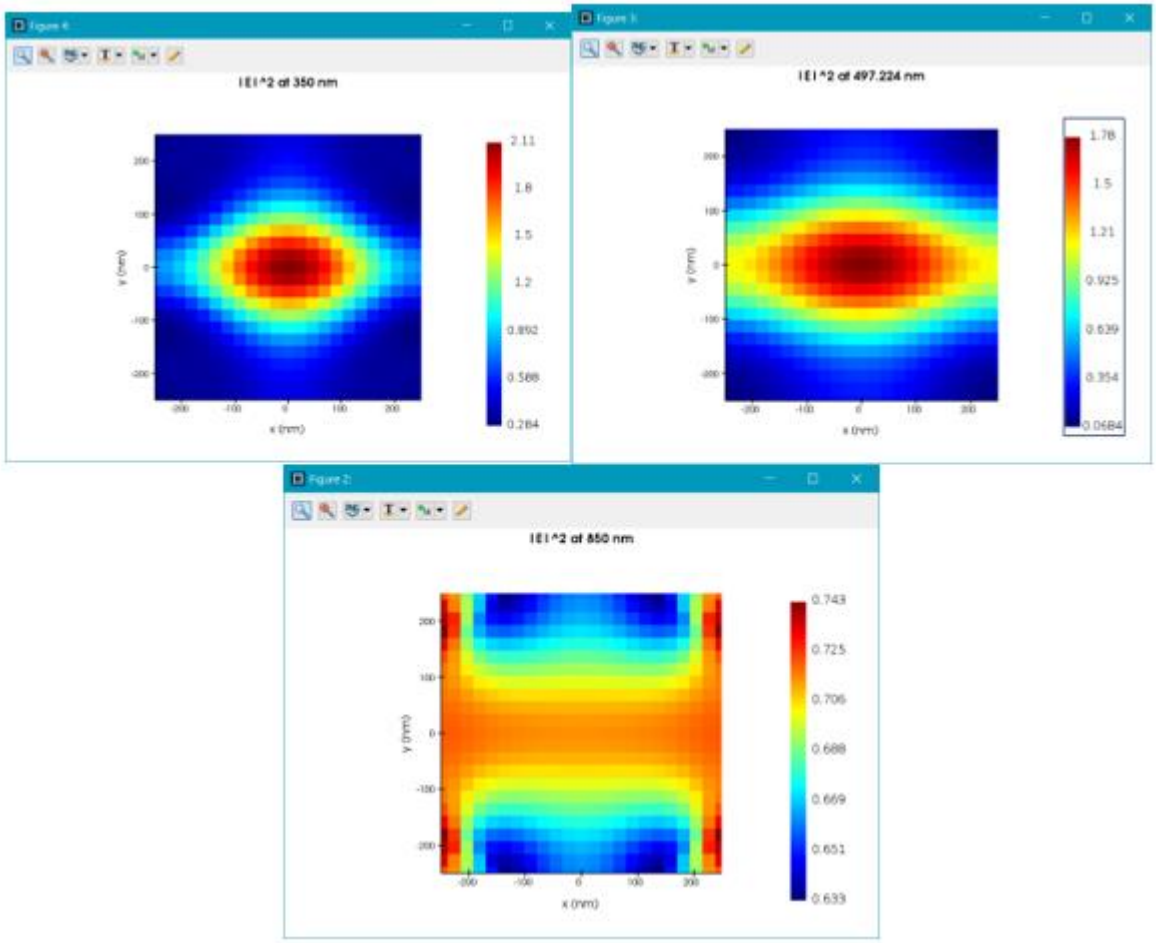

Figure6.8 Intensity (|E|^2) profile plots at the minimum, maximum and center wavelengths

6.2.4 *Glass (SiO2) Substrate and PMSSQ Moth-Eye Structures, Radius of Curvature = 200nm, Pitch = 500nm.*

In this design, when trying to change the pitch size between the consecutive nipple-structures, a small variation was given with a difference of pitch length of 5nm.

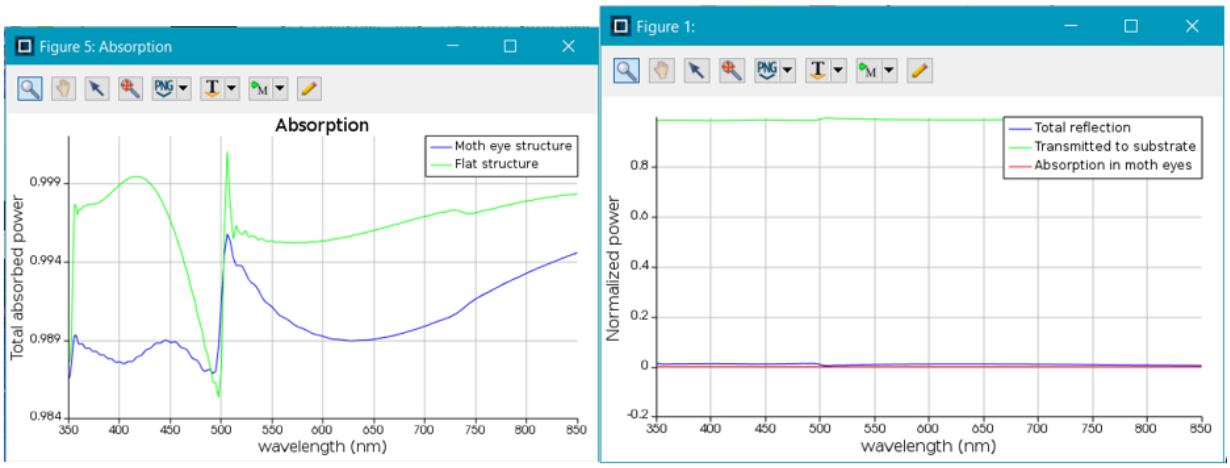

Figure 6.9 (a) normalized power and (b) absorption power absorption graph for SiO2 substrates with PMSSQ moth-eyed structure for radius of 200nm and pitch size of 500nm.

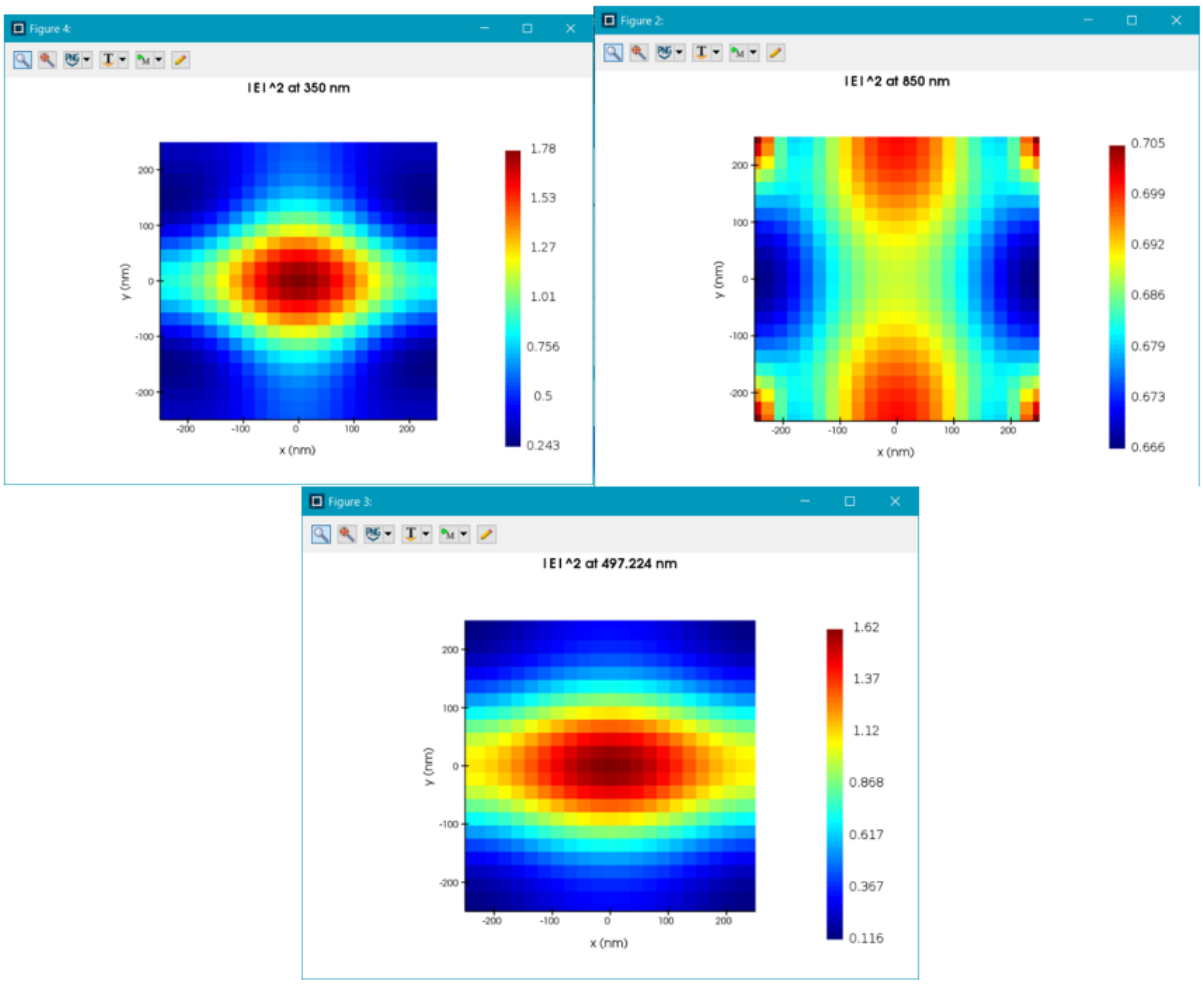

Figure 6.10 Intensity (|E|^2) profile plots at the minimum, maximum and center wavelengths

6.2.5 *Glass (SiO2) Substrate and PMSSQ Moth-Eye Structures, Radius of Curvature = 200nm, Pitch = 505nm.*

Similar results were obtained, when altering the pitch size here as well.

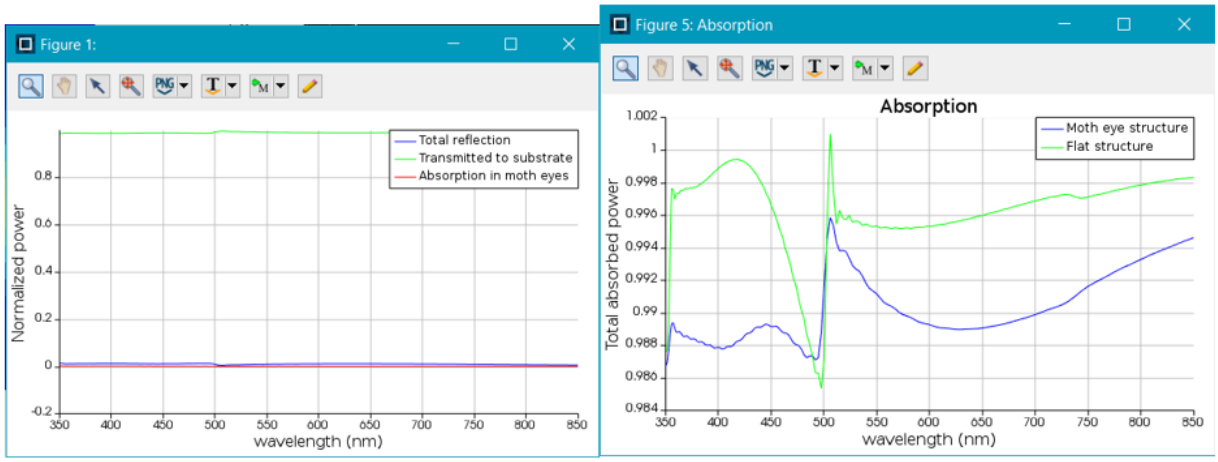

Figure 6.11 (a) normalized power and (b) absorption power absorption graph for SiO2 substrates with PMSSQ moth-eyed structure for radius of 200nm and pitch size of 505nm.

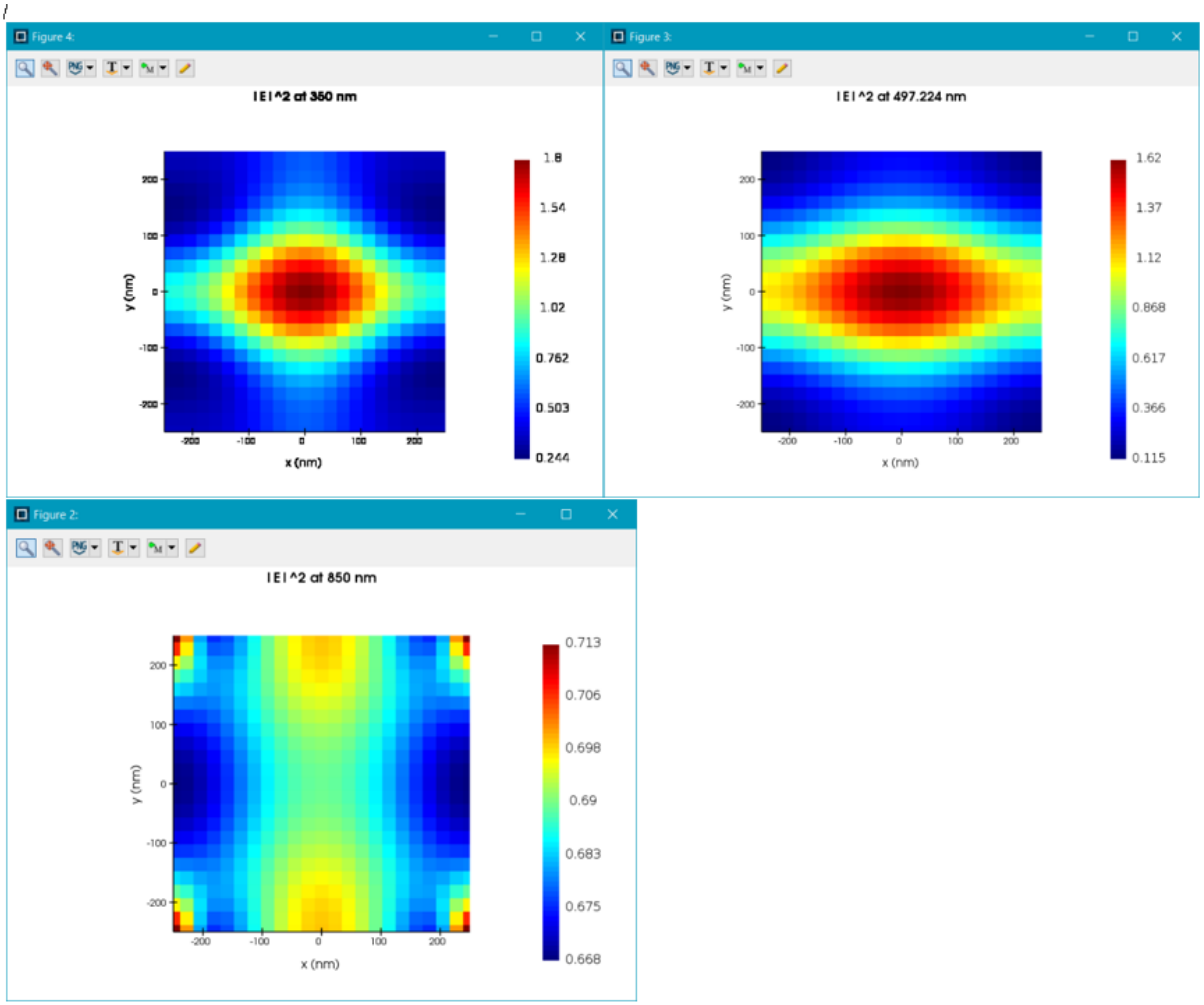

Figure 6.12 Intensity (|E|^2) profile plots at the minimum, maximum and center wavelengths

7. CONCLUSION AND FUTURE WORK

We have thus reached the end of this report to give a summary of the work that has been carried out as part of this research work. An easy self-assembly technique along with the microfabrication techniques required to work in the clean room has also been detailed here. The primary focus of this research was to build subwavelength nanostructures in the range of 200nm, to get a graded refractive index that could be employed to a broadband of incident wavelengths. The results obtained through reactive ion etching using various etch recipes have been studied in detail in this report. Although the result obtained through chlorine etch studies would have taken this research another step, we were still able to recreate the required results with available resources.

We were able to get our desired structures using the two-step reactive ion etching process, which proved valuable for us to move on to the next step. However, this did not meet our need of a large-scale fabrication and thus drove the development of a novel means of fabricating the obtained structures on large-area substrate like glass, as most of the applications with anti-reflection would be on glass. This novel method involved the use of a simple and easy roll-to-roll technique.This, along with timely studies using simulation models, has helped in getting better results on what to expect from working on it hands-on.

As part of future work, this design could be done studying more on the etching process to obtain even smaller feature sized nanostructures with greater depth and etch studies. More research

can be done in demonstrating better and faster etch results for obtaining the nanostructures effectively. Additionally, further development of the replica hard mask for nanotransferring the already-etched structures can be done. There are still challenges due to anti-reflection materials and the large-scale development for the same. This proven method can aid in saving time and money for increasing productivity for the required applications.

REFERENCES

[1] Steiner, Ullrich, et al. "Process for producing antireflection coatings." U.S. Patent No. 6,605,229. 12 Aug. 2003.

[2] Yoldas, Bulent E., and Deborah P. Partlow. "Antireflective graded index silica coating, method for making." U.S. Patent No. 4,535,026. 13 Aug. 1985.

[3] Lohmüller, Theobald, et al. "Biomimetic interfaces for high-performance optics in the deep-UV light range." *Nano Letters* 8.5 (2008): 1429-1433.

[4] Raut, Hemant Kumar, et al. "Multiscale ommatidial arrays with broadband and omnidirectional antireflection and antifogging properties by sacrificial layer mediated nanoimprinting." *ACS Nano* 9.2 (2015): 1305-1314.

[5] Sun, Chih-Hung, Peng Jiang, and Bin Jiang. "Broadband moth-eye antireflection coatings on silicon." *Applied Physics Letters* 92.6 (2008): 061112.

[6] Asadollahbaik, Asa, et al. "Reflectance properties of silicon moth-eyes in response to variations in angle of incidence, polarisation and azimuth orientation." *Optics Express* 22.102 (2014): A402-A415.

[7] Wilson, S. J., and M. C. Hutley. "The optical properties of'moth eye'antireflection surfaces." *Optica Acta: International Journal of Optics* 29.7 (1982): 993-1009.

[8] Lohmueller, Theobald, Robert Brunner, and Joachim P. Spatz. "Improved properties of optical surfaces by following the example of the 'Moth Eye'." *Biomimetics Learning From Nature* (2010), pp, 451-453

[9] Yasmeen, Sadaf, et al. "Synthesis, structural and optical analysis of surfactant assisted ZnO–NiO nanocomposites prepared by homogeneous precipitation method." *Ceramics International* 45.14 (2019): 17859-17873.

[10] Raut, Hemant Kumar, et al. "Anti-reflective coatings: A critical, in-depth review." *Energy & Environmental Science* 4.10 (2011): 3779-3804.

[11] Colson, P., et al. "Nanosphere Lithography: A Powerful Method for the Controlled Manufacturing of Nanomaterials, Nanosphere Lithography: A Powerful Method for the Controlled Manufacturing of Nanomaterials." *J. Nanomater* 2013 (2013): e948510.

[12] Park, Jin Young, and Rigoberto C. Advincula. "Nanostructuring polymers, colloids, and nanomaterials at the air–water interface through Langmuir and Langmuir–Blodgett techniques." *Soft Matter* 7.21 (2011): 9829-9843.

[13] Fendler, J., and H. Janos, eds. *Nanoparticles and nanostructured films: preparation, characterization, and applications*. John Wiley & Sons, 2008.

[14] Korampally, Venumadhav, et al. "Entropy driven spontaneous formation of highly porous films from polymer–nanoparticle composites." *Nanotechnology* 20.42 (2009): 425602.

[15] Sankabathula, Giridhar Tulasi Ram, 2020, "Shape Tuning of Silicon Nano-tip Arrays Through Reactive Ion Etching for Cold Field Emission", M.S. Thesis, Northern Illinois University, Dekalb, IL

[16] Korampally, Venumadhav, et al. "Sub-minute formation of supported nanoporous mesoscale patterns programmed by surface energy." *Journal of colloid and interface science* 364.2 (2011): 546-554.

[17] Park, Min Soo, Youngmin Lee, and Jin Kon Kim. "One-step preparation of antireflection film by spin-coating of polymer/solvent/nonsolvent ternary system." *Chemistry of Materials* 17.15 (2005): 3944-3950.

[18] Nayak, A. P., M. S. Islam, and V. J. Logeeswaran. "Dry Etching." *Encyclopedia of Nanotechnology*. Springer, Netherlands (2012): 587-589.

[19] Buchine, Brent A., Faris Modawar, and Marcie R. Black. "Process for fabricating nanowire arrays." U.S. Patent No. 8,143,143. 27 Mar. 2012.

[20] d'Agostino, Riccardo, and Daniel L. Flamm. "Plasma etching of Si and SiO2 in SF6–O2 mixtures." *Journal of Applied Physics* 52.1 (1981): 162-167.

[21] Saloum, Saker, et al. "Silicon nanostructuring using SF6/O2 downstram plasma etching: morphological, optical and sensing properties." *Materials Research* 21.5 (2018).

[22] Lan, Hongbo. "Large-Area nanoimprint lithography and applications." *Micro/Nanolithography-A heuristic aspect on the enduring technology* (2018): 43-68.